

NAVAL POSTGRADUATE SCHOOL

Monterey, California



THESIS

**ANALYSIS OF THE TRANSITION IN DEFORMATION
MECHANISMS IN SUPERPLASTIC 5083 ALUMINUM
ALLOYS BY ORIENTATION IMAGING MICROSCOPY**

by

James William Harrell

September 2001

Thesis Advisor:

Terry R. McNelley

Approved for public release; distribution is unlimited

THIS PAGE INTENTIONALLY LEFT BLANK

REPORT DOCUMENTATION PAGE			<i>Form Approved OMB No. 0704-0188</i>	
Public reporting burden for this collection of information is estimated to average 1 hour per response, including the time for reviewing instruction, searching existing data sources, gathering and maintaining the data needed, and completing and reviewing the collection of information. Send comments regarding this burden estimate or any other aspect of this collection of information, including suggestions for reducing this burden, to Washington headquarters Services, Directorate for Information Operations and Reports, 1215 Jefferson Davis Highway, Suite 1204, Arlington, VA 22202-4302, and to the Office of Management and Budget, Paperwork Reduction Project (0704-0188) Washington DC 20503.				
1. AGENCY USE ONLY (Leave blank)		2. REPORT DATE September 2001	3. REPORT TYPE AND DATES COVERED Master's Thesis	
4. TITLE AND SUBTITLE: Title (Mix case letters) Analysis of the Transition in Deformation Mechanisms in Superplastic 5083 Aluminum Alloys by Orientation Imaging Microscopy			5. FUNDING NUMBERS	
6. AUTHOR(S) Harrell, James W.				
7. PERFORMING ORGANIZATION NAME(S) AND ADDRESS(ES) Naval Postgraduate School Monterey, CA 93943-5000			8. PERFORMING ORGANIZATION REPORT NUMBER	
9. SPONSORING / MONITORING AGENCY NAME(S) AND ADDRESS(ES) General Motors Corp., Research and Development Center, Warren, MI (Dr. Paul E. Krajewski, Technical Program Monitor), under subcontract with Univ. of Texas-Austin (Prof. Eric Taleff)			10. SPONSORING / MONITORING AGENCY REPORT NUMBER	
11. SUPPLEMENTARY NOTES The views expressed in this thesis are those of the author and do not reflect the official policy or position of the Department of Defense or the U.S. Government.				
12a. DISTRIBUTION / AVAILABILITY STATEMENT Approved for public release; distribution is unlimited			12b. DISTRIBUTION CODE	
13. ABSTRACT (maximum 200 words) Recently developed Orientation Imaging Microscopy (OIM) methods have been applied to the analysis of microstructure and microtexture of 5083 aluminum alloy materials that have been processed to enable superplasticity. The phenomenon of superplasticity allows economical forming of complex components while retaining the high strength- and stiffness-to-weight ratios characteristic of aluminum alloys used in automotive, aerospace and military applications. Superplasticity requires fine grains with high-angle boundaries and resistance to failure by cavitation. OIM permits grain-specific orientation determination and quantitative assessment of the grain-to-grain disorientation distribution as well as grain size measurement in materials. The current work offers significant new insights into the development and response of superplastic microstructures; in particular, OIM data may be employed to delineate the transition from slip to grain boundary sliding in superplastic 5083 materials.				
14. SUBJECT TERMS Superplasticity, Orientation Imaging Microscopy, Deformation Mechanism Grain Boundary Sliding, Dislocation Creep, Microstructure, Microtexture, Disorientation Angle			15. NUMBER OF PAGES 95	
			16. PRICE CODE	
17. SECURITY CLASSIFICATION OF REPORT Unclassified	18. SECURITY CLASSIFICATION OF THIS PAGE Unclassified	19. SECURITY CLASSIFICATION OF ABSTRACT Unclassified	20. LIMITATION OF ABSTRACT UL	

THIS PAGE INTENTIONALLY LEFT BLANK

Approved for public release; distribution is unlimited

**ANALYSIS OF THE TRANSITION IN DEFORMATION MECHANISMS IN
SUPERPLASTIC 5083 ALUMINUM ALLOYS BY ORIENTATION IMAGING
MICROSCOPY**

James W. Harrell
Lieutenant, United States Navy
B.S., United States Naval Academy, 1994

Submitted in partial fulfillment of the
requirements for the degree of

**MASTER OF SCIENCE IN
MECHANICAL ENGINEERING**

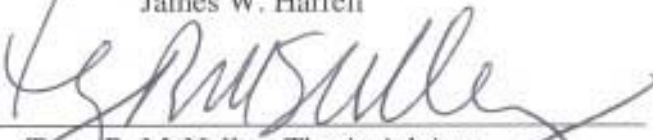
from the

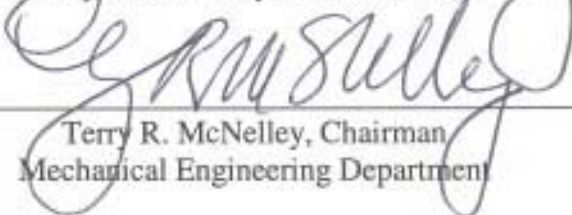
**NAVAL POSTGRADUATE SCHOOL
September 2001**

Author:


James W. Harrell

Approved by:


Terry R. McNelley, Thesis Advisor


Terry R. McNelley, Chairman
Mechanical Engineering Department

THIS PAGE INTENTIONALLY LEFT BLANK

ABSTRACT

Recently developed Orientation Imaging Microscopy (OIM) methods have been applied to the analysis of microstructure and microtexture of 5083 aluminum alloy materials that have been processed to enable superplasticity. The phenomenon of superplasticity allows economical forming of complex components while retaining the high strength- and stiffness-to-weight ratios characteristic of aluminum alloys used in automotive, aerospace and military applications. Superplasticity requires fine grains with high-angle boundaries and resistance to failure by cavitation. OIM permits grain-specific orientation determination and quantitative assessment of the grain-to-grain disorientation distribution as well as grain size measurement in materials. The current work offers significant new insights into the development and response of superplastic microstructures; in particular, OIM data may be employed to delineate the transition from slip to grain boundary sliding in superplastic 5083 materials.

THIS PAGE INTENTIONALLY LEFT BLANK

TABLE OF CONTENTS

I. INTRODUCTION	1
II. BACKGROUND.....	5
A. SUPERPLASTICITY AND DEFORMATION MECHANISMS	5
B. PRIOR STUDY OF SUPERPLASTIC SKY 5083 ALUMINUM ALLOYS	9
C. DEFINITION OF GRAIN BOUNDARY DISORIENTATION IN OIM... 10	
D. BACKGROUND ON MECHANICAL TESTING PROCEDURES FOR THE 978901 AND 978083 AA5083 MATERIALS	16
III. EXPERIMENTAL PROCEDURES.....	19
A. OVERVIEW	19
B. MATERIALS.....	20
C. ANNEALING OF SAMPLES.....	21
D. SAMPLE PREPARATION FOR OIM.....	21
E. ELECTRON BACKSCATTER DIFFRACTION PATTERN COLLECTION.....	25
F. ORIENTATION IMAGING MICROSCOPY ANALYSIS	30
G. OPTICAL MICROSCOPY.....	34
IV. RESULTS AND DISCUSSION.....	35
A. THE AS-RECEIVED CONDITION OF THE 978901 AND 978083 AA5083 ALLOY MATERIALS.....	35
B. EFFECT OF ANNEALING ON THE 978901 AND 978083 MATERIALS.....	43
C. MECHANICAL TESTING OF 5083 ALUMINUM ALLOYS 978901 AND 978083	56
D. OIM AND MICROTEXTURE ANALYSIS OF 5083 ALUMINUM ALLOYS 978901 AND 978083 AFTER TENSILE DEFORMATION....	57
E. OIM AND MICROTEXTURE ANALYSIS OF SKY 5083 ALUMINUM ALLOYS AFTER TENSILE DEFORMATION	71
V. CONCLUSIONS.....	77
A. CONCLUSIONS.....	77
B. APPLICATION OF OIM TO MODELING OF SUPERPLASTIC RESPONSE.....	78
C. RECOMMENDATIONS FOR FURTHER STUDY	79
LIST OF REFERENCES	81
INITIAL DISTRIBUTION LIST	83

THIS PAGE INTENTIONALLY LEFT BLANK

ACKNOWLEDGMENTS

The author wishes to extend his strongest appreciation to Professor Terry McNelley for his guidance during this work. The author would also like to thank Doug Swisher, Dr. Chan Park, Mary-Anne Kulas, and Tracy Maestas for their contributions.

Finally, the author wishes to recognize and thank his family, Chris and Jake, for their inspiration and support during the long hours dedicated to this project.

THIS PAGE INTENTIONALLY LEFT BLANK

I. INTRODUCTION

Weight reduction in structural components has always been of great concern for engineers engaged in design of transportation and other systems. A reduction in weight while maintaining strength requirements generally results in a reduction in energy required to move such systems. In today's world of decreasing energy supplies and increasing energy cost, the demand for machines that are capable of doing the same job at lower energy cost will continue to rise.

Substitution of aluminum alloys for steels is one method by which weight saving may be realized. Ashby [Ref. 1] has developed methods for ranking and comparing materials for structural applications. Thus, for deflection-limited design of components subjected to flexure the substitution of aluminum for steel provides a theoretical 40% weight savings while the same substitution in a component subjected to a distributed load can provide a theoretical weight savings of 30%.

Many factors play a role in the selection of materials for specific components. Aluminum alloys have not been used more widely for many structural and transportation applications because alloys of sufficient strength may be difficult to form using conventional die forming methods, and alloys that are easily formed often do not possess sufficient strength. In the aerospace industry, weight is especially critical and high-strength aluminum alloys are widely used despite higher costs associated with forming and fabrication. Improved forming characteristics in high-strength aluminum alloys would enable design simplification and further weight savings for aerospace as well as general transportation applications.

Superplastic forming offers an alternative to traditional sheet forming techniques and is capable of shaping higher strength aluminum alloys. This method requires heating to high temperatures (generally $\geq 425^{\circ}\text{C}$) and use of slow strain rates (1×10^{-4} to $1 \times 10^{-3} \text{ s}^{-1}$) to achieve the exceptional ductility associated with this phenomenon [Ref. 2]. Unlike closed-die pressing, superplastic forming requires minimal work input. Superplastic forming is typically accomplished by subjecting a heated sheet of superplastic material to a pressure differential in a chamber as illustrated in the schematic in Figure 1.1. The

sheet initially deforms under biaxial tension as a membrane until it comes in contact with the die; the subsequent flow behavior may then become quite complex. Because the strain rate must remain low, long forming times result and the associated costs may be of concern. However, the dies needed for superplastic forming do not require the same strength and hardness as those used for sheet forming and may therefore be less expensive to fabricate or purchase. The requirement to operate multiple superplastic forming presses in order to achieve the desired production rate may be an additional cost factor.

Among the many issues involved in expanding the utilization of superplastic forming is the need to achieve better understanding of the relationships among alloy constitution, material processing, microstructure and superplastic response. Recently developed Orientation Imaging Microscopy (OIM) techniques permit detailed study of microstructure, and especially the nature of grain boundaries, as well as new capability in the characterization of deformation mechanisms. This research has focused primarily on this technique and its application to superplastic aluminum alloys. The current work has expanded on previous electron backscatter diffraction (EBSD) investigations into the behavior of a proprietary SKY5083 aluminum alloy [Refs. 3-5]. Two new AA5083 aluminum alloy compositions, designated as lots 978083 and 978901, were the primary focus of this study. The 978083 material gave twice the maximum superplastic elongation as the 978901 material. These materials were studied in the as-received, annealed, and deformed conditions in an attempt to clarify the reasons for the differences in superplastic response.

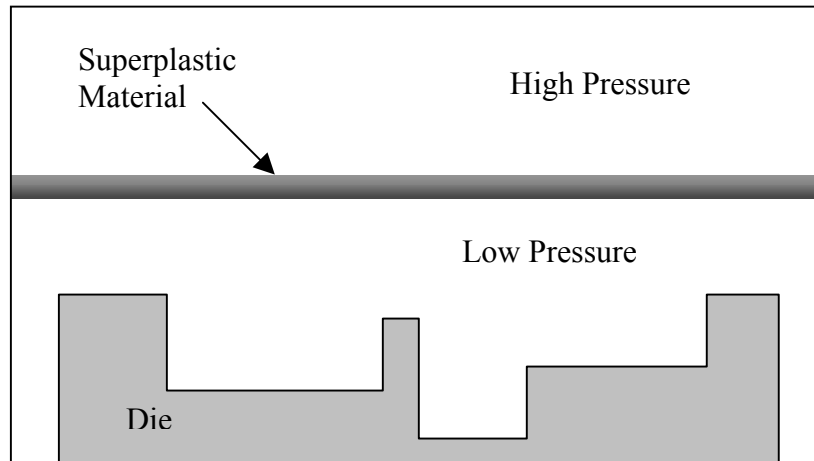


Figure 1.1 Schematic of superplastic forming. Material is driven to conform to the die's shape by a pressure difference in the forming chamber. Superplastic forming, while slower than conventional closed-die forming, requires less costly dies and support facilities and is competitive for many applications.

THIS PAGE INTENTIONALLY LEFT BLANK

II. BACKGROUND

A. SUPERPLASTICITY AND DEFORMATION MECHANISMS

Superplasticity is the ability of a polycrystalline material to undergo extreme, neck-free tensile elongation. Engineering metals typically exhibit tensile elongations of 10% to 100%; elongation values $\geq 200\%$ are considered superplastic and elongation values of 1000% or more are not uncommon. Superplastic behavior has been observed in ceramic and composite materials as well as metals [Ref. 2].

From the perspective of applied mechanics, superplasticity may be understood on the basis of the material's stress versus strain-rate relationship, which may be assumed to be of the form:

$$\sigma = K\dot{\epsilon}^m \quad \text{Equation 2.1}$$

where σ is the flow stress, K is a material constant, $\dot{\epsilon}$ is the strain rate and m is the strain-rate sensitivity coefficient. At the onset of necking in the deforming gage section of a tensile sample the localized deformation results in a local increase in strain rate in the neck. A large value of the strain rate sensitivity coefficient, m , increases the resistance to further localized deformation in the neck. Thus, large m values lead to uniform deformation and thereby result in enhanced tensile ductility. Newtonian viscous behavior, which occurs in glass deformed near its melting point, corresponds to a value of $m = 1$, which, in turn, gives extreme resistance to localized necking and failure. Most polycrystalline metals exhibit $m \leq 0.2$ during elevated temperature deformation and elongation-to-failure values are generally $\leq 100\%$. For superplastic materials, m values are typically 0.33 - 0.5 [Ref. 2]; such values result in sufficient resistance to necking to enable superplastic response. Large values of the strain rate sensitivity coefficient, m , are necessary but not sufficient to assure superplastic response. The material must also resist the formation and linkage of cavities, which may lead to premature failure in superplastic materials.

Materials that have been processed for superplastic behavior often exhibit varying values of m as a function of strain rate during testing at a given, constant temperature.

Figure 2.1 illustrates this for a hypothetical material that exhibits an m value of 0.5 at lower strain rates and 0.2 at higher strain rates. This circumstance may arise when two independent deformation mechanisms contribute to the elevated temperature deformation of the material. Thus, grain boundary sliding (GBS), accommodated by slip, and dislocation creep occur independently, and both may take place during elevated temperature deformation. Because they occur independently their effects are additive. The overall material response is determined by the sum of the strain rate due to GBS and the strain rate due to dislocation creep; the mechanism that gives the fastest strain rate will apparently dominate [Ref. 6]. As suggested in Figure 2.1, GBS ($m = 0.5$) dominates at low strain rates and the material exhibits superplastic ductility. At high strain rates, dislocation creep ($m = 0.2$) dominates, and this results in normal ductility. As seen in the plot of Figure 2.1, the region of transition from superplastic to normal ductility spans about one to two orders of magnitude in strain rate [Ref. 7].

Several models have been proposed to describe the additive contributions of GBS and dislocation creep. These models generally assume that each mechanism may be described by a relationship similar to that of Equation 2.1, but assigning the appropriate values of K and m for the individual terms based on the deformation mechanism. One such model is [Refs. 2,5,7,8],

$$\frac{\dot{\epsilon}}{D_L} = \frac{10^{11}}{b^2} \left(\frac{\sigma}{E} \right)^5 + \frac{2 \times 10^9}{L^2} \left(\frac{\sigma}{E} \right)^2 \quad \text{Equation 2.2}$$

where D_L is lattice diffusivity, b is the Burger's vector, L is the mean linear intercept grain size, and E is Young's modulus. The first term on the right is the contribution of dislocation creep, which is independent of grain size. The exponent of 5 in this term is the reciprocal of the strain rate sensitivity coefficient and so $m = 0.2$ if this term predominates. The second term on the right describes GBS, which is grain-size dependent. The exponent of 2 gives $m = 0.5$ and superplastic ductility when this term predominates.

At a constant temperature, there is a maximum strain rate at which superplastic behavior may be observed which corresponds to the transition point identified in Figure 2.1. To increase the practicality of superplastic forming the strain rate at which this

transition occurs should be maximized. This may be accomplished by processing to refine the grain size; a reduction in grain size, L , increases the contribution of the GBS term in Equation 2.2 and thus the strain rate for the transition from GBS to dislocation creep.

A refined and stable grain structure, which is rich in high angle boundaries, is thus a prerequisite for superplasticity [Refs. 8,9]. GBS is concentrated at the grain boundaries and in a mantle-like region in the vicinity of the boundaries [Refs. 10,11]. In general, the maximum strain rate at which GBS is possible is inversely proportional to the grain size raised to a power of two or three [Ref. 12]. For this reason it is necessary to control grain growth, which can be accomplished by addition of second phase particles to inhibit grain boundary migration. High angle boundaries are also required to enable sliding [Ref. 13]. High-angle boundaries can slide more readily than low-angle boundaries, which do not slide readily due to coherency across the grain boundaries. An equiaxed grain structure will enable GBS better than an elongated structure [Ref. 2]. A random texture is thought to favor GBS. Finally, mobile grain boundaries will allow the relaxation of stress concentrations at triple points and other obstructions and permit the structure to remain equiaxed and avoid the formation of cavities.

A fine-grained microstructure rich in high angle boundaries can be produced by introducing a dispersion of second phase particles sufficient to serve as sites for particle-stimulated nucleation (PSN) of recrystallization. In PSN, high angle boundaries are formed in deformation zones around the second phase particles, which must exceed a certain size, typically about $1.0\text{ }\mu\text{m}$, in order to become nucleation sites [Refs. 14-17]. If well dispersed, such second phase particles will result in a fine and equiaxed microstructure. In general, PSN results in a randomly textured material due to the randomizing of lattice orientations within deformation zones around the second-phase particles [Ref. 14]. It has also been suggested that fine, dispersed particles possessing a higher hardness than the matrix can control cavitation by various recovery mechanism near the particle [Ref. 18].

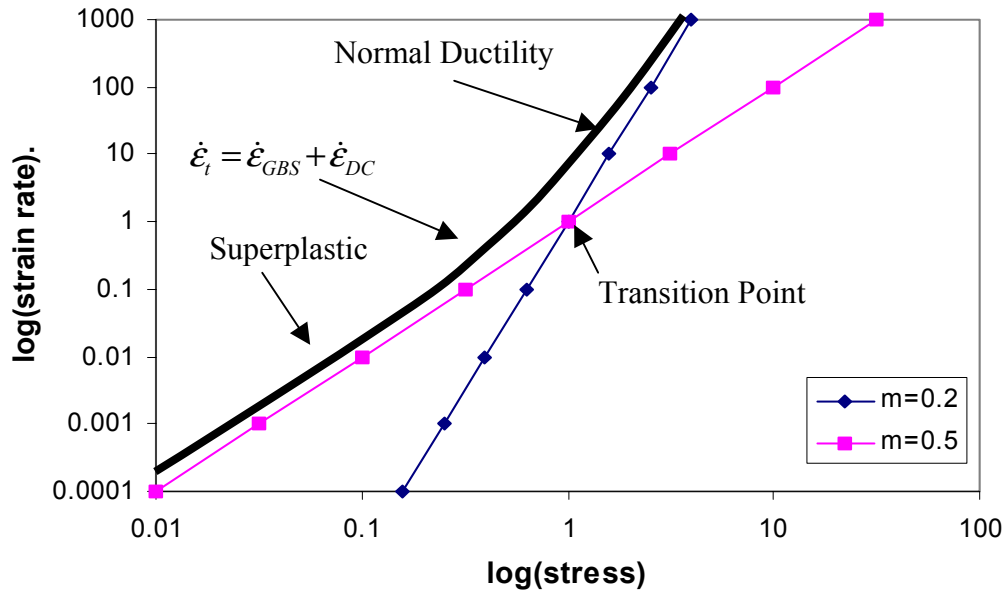


Figure 2.1 Schematic plot of $\log(\text{stress})$ vs. $\log(\text{strain rate})$ for $m=0.2$ corresponding to normal ductility and $m=0.5$ corresponding to superplastic ductility. The overall strain rate response is the sum of the strain rate response for superplastic and dislocation creep mechanisms. The transition from GBS dominated to dislocation creep dominated response spans only a single order of magnitude.

B. PRIOR STUDY OF SUPERPLASTIC SKY 5083 ALUMINUM ALLOYS

OIM analysis was conducted on SKY 5083 aluminum alloy as part of the current effort in order to validate prior work and to assess a superplastic material that had been deformed over a wide range of strain rates. Deformed samples of this material were available from previous study at the Naval Postgraduate School. SKY 5083 material is a proprietary product processed for a stable fine grain structure capable of superplastic forming. The specific processing details are proprietary. However, it is assumed that the material is cold rolled following the development of a distribution of Al_6Mn particles that provide sites for particle stimulated nucleation of recrystallization during annealing after deformation processing. The chemical composition of the alloy is provided in Table 2.1. Tensile testing was accomplished in previous work following initial annealing of the test coupons at 535 °C for 30 minutes in order to produce a fine, equiaxed and stable grain structure. Tension tests were then conducted at constant crosshead speed to failure at a variety of nominal strain rates and temperatures [Refs. 3-5].

The analysis method used in the prior work involved an interactive computer-aided electron backscatter method [Refs. 3,4]. The data collection method was not as fully automated as it is in OIM. In this prior work, the electron beam was manually displaced across the sample surface and data points were recorded only when a change in diffraction pattern was observed; a typical data set involved only about 500 orientation measurements, which allowed assessment of microtexture and grain-to-grain disorientations. Data sets obtained in the current OIM study typically involve approximately 11,000 orientation measurements and data representations that include orientation-based images as well as microtexture analysis.

The texture of the annealed SKY5083 was predominantly random, although a weak $\{001\}$ cube-type component could also be discerned in the data. The essential results of the investigation of the SKY material that had been deformed at 535°C are summarized in Figure 2.2. [Ref. 5] These discrete pole figures show the difference in microtexture resulting from deformation in the superplastic regime when compared to deformation in the dislocation creep regime. Following deformation in the superplastic regime, the texture of the material became essentially completely random.

This was associated with random grain rotations during GBS. Following deformation in the dislocation creep regime, preferred orientations became apparent in the texture data: a $\langle 111 \rangle$ fiber orientation and a $\{100\}\langle 100 \rangle$ cube component. Analysis of slip processes in these two components demonstrated that they are mutually compatible with uniaxial tensile deformation. It was proposed that the $\langle 111 \rangle$ fiber component evolved from the random grains while the $\{100\}\langle 001 \rangle$ cube component developed from grains in the $\{001\}\langle uv0 \rangle$ population. A schematic diagram of the evolution of these features of the microtexture is shown in Figure 2.3. [Ref. 5]

The study concluded that dislocation creep and GBS deformation mechanisms contribute independently and additively to the deformation rate and that the dominant deformation mechanism in a superplastically deformed material can be inferred from the texture changes that occur during straining.

Mg	Mn	Cr	Fe	Si	Al
4.48	0.65	0.11	0.07	0.05	Bal.

Table 2.1. Alloy composition (wt%) of SKY 5083 Aluminum alloy. After Ref. [5].

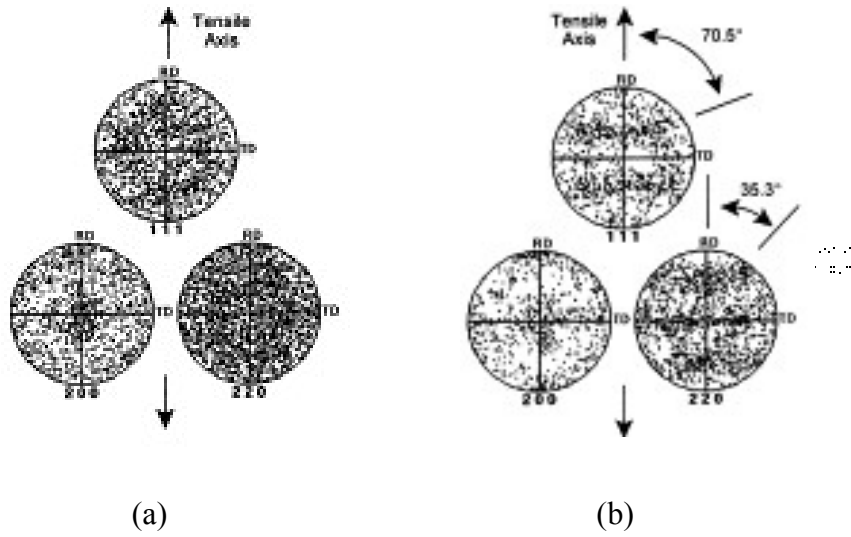


Figure 2.2 Discrete pole figures for SKY 5083 aluminum alloy deformed at 535°C at (a) $1 \times 10^{-4} \text{ s}^{-1}$ in the GBS regime and (b) $1 \times 10^{-1} \text{ s}^{-1}$ in the dislocation creep regime. In the GBS regime, a randomization of the texture occurs. In the dislocation creep regime, a preferred texture including $\{100\}\langle 001 \rangle$ cube component and $\langle 111 \rangle$ fiber component. From Ref. [5].

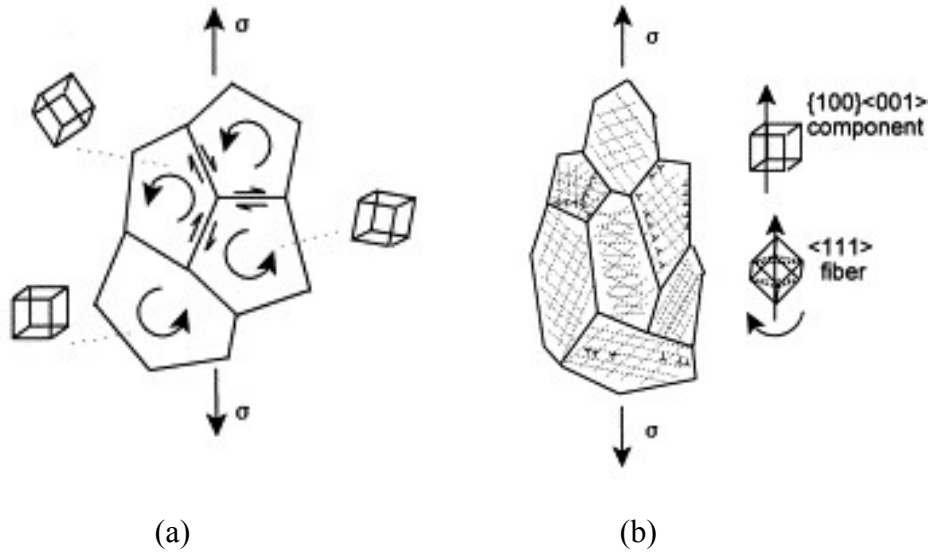


Figure 2.3. Schematic diagrams of the microstructural effect of (a) GBS and (b) dislocation creep deformation mechanisms. From Ref. [5].

C. DEFINITION OF GRAIN BOUNDARY DISORIENTATION IN OIM

Sample preparation and detailed procedures for OIM data acquisition and analysis will be provided in Chapter III. High-angle grain boundaries are necessary for superplasticity and evaluation of the distribution of the grain-to-grain disorientations and their statistical significance in superplastic materials is feasible using OIM. The electron beam of a scanning electron microscope (SEM) may be used as a probe of local lattice orientation at a point within the grain structure of a material [Ref. 19]. In OIM, the electron beam is displaced, point-by-point, in a raster pattern on the surface of a material sample and the lattice orientation is determined at each point in the raster. The resulting data file may be analyzed to produce an orientation-based image of the microstructure. In such a procedure, the applicable definition of a grain is a region of constant lattice orientation within a specified orientation tolerance. Then, grain boundaries separate regions of different lattice orientation. If the lattice orientations of two adjacent points are known, the disorientation angle between them may be computed. Figure 2.4 is a schematic illustration of the lattice orientations of two orientations that lie in adjacent grains. First, by selecting a grain tolerance angle, one defines the maximum disorientation between two points that may be considered part of the same grain. Then, by compiling disorientation data between all points, one may assemble a grain map that will illustrate level of grain refinement and a distribution of high angle boundaries.

The disorientation is defined as the smallest among all crystallographically equivalent rotations that bring two lattices into coincidence. Figure 2.5 shows two lattices that are disoriented by an angle ϕ about the Z-axis. This rotation could also be described $\pi/2 - \phi$, $\pi - \phi$, or $3\pi/2 - \phi$ about the Z-axis. In general, there are up to 24 possible rotations that can describe the same disorientation in a cubic lattice. By convention, the disorientation is taken as the smallest absolute rotation [Ref. 19].

The computation of the disorientations requires that all orientations be expressed in a common reference axis system. This axis system is commonly defined for rolled materials as the x_1 axis parallel to the rolling direction (RD), x_2 parallel to the transverse direction (TD), and x_3 parallel to the normal direction (ND) [Ref. 19]. Then, three Euler angles (ϕ_1 , Φ , ϕ_2) are used to describe the sequence of three rotations that are required to

bring the cube axes of a cubic lattice into coincidence with these reference directions. Bunge's convention is used to construct the Euler angles with ϕ_1 being the first rotation about the crystal x_3 axis, Φ being a subsequent rotation about the crystal x_1 axis, and ϕ_2 being a second rotation about the crystal x_3 axis [Refs. 19,20].

Using these conventions, any lattice orientation can be described with respect to the reference system. To determine the disorientation angle, orientation matrices are constructed for each of two adjacent lattice orientation measurements. The orientation matrix $[A_1]$ for the first one is given by:

$$[A_1] = \begin{bmatrix} \cos \phi_1 \cos \phi_2 - \sin \phi_1 \sin \phi_2 \cos \Phi & \sin \phi_1 \cos \phi_2 + \cos \phi_1 \sin \phi_2 \cos \Phi & \sin \phi_2 \sin \Phi \\ -\cos \phi_1 \sin \phi_2 - \sin \phi_1 \cos \phi_2 \cos \Phi & -\sin \phi_1 \sin \phi_2 + \cos \phi_1 \cos \phi_2 \cos \Phi & \cos \phi_2 \sin \Phi \\ \sin \phi_1 \sin \Phi & -\cos \phi_1 \sin \Phi & \cos \Phi \end{bmatrix} \quad \text{Equation 2.3}$$

A corresponding matrix $[A_2]$ is computed for the next, and then the rotations may be determined by:

$$[M] = [A_1]^{-1} [A_2] \quad \text{Equation 2.4}$$

There are up to 24 crystallographically equivalent rotation matrices $[M]$. The disorientation may be found by a minimization operation among the corresponding rotation angles, i.e., the disorientation is given by:

$$\theta_{12} = \min \left| \arccos \left[\frac{1}{2} (m_{11}^{12} + m_{22}^{12} + m_{33}^{12} - 1) \right] \right| \quad \text{Equation 2.5}$$

where the m_{ij} terms correspond to the diagonal terms of the $[M]$ giving the smallest θ . For this definition, θ has the range $0^\circ - 62.8^\circ$. If the θ value between any two neighboring orientation measurements is less than the grain tolerance angle, the points will be considered part of the same grain. Once the lattice orientations for adjacent grains have been determined the grain-to-grain disorientation may also be determined.

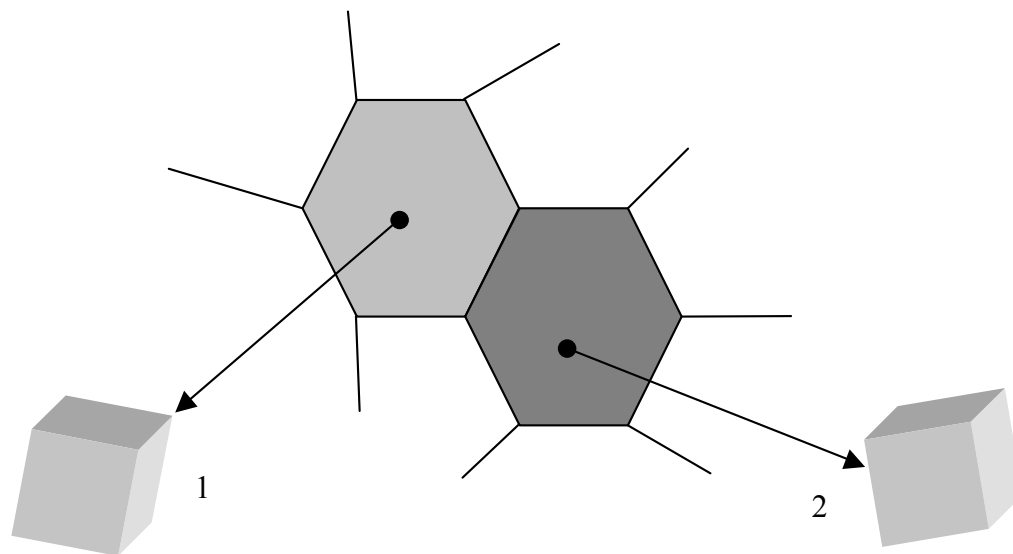


Figure 2.4. Schematic of adjacent grains illustrating the disorientation between the lattices.

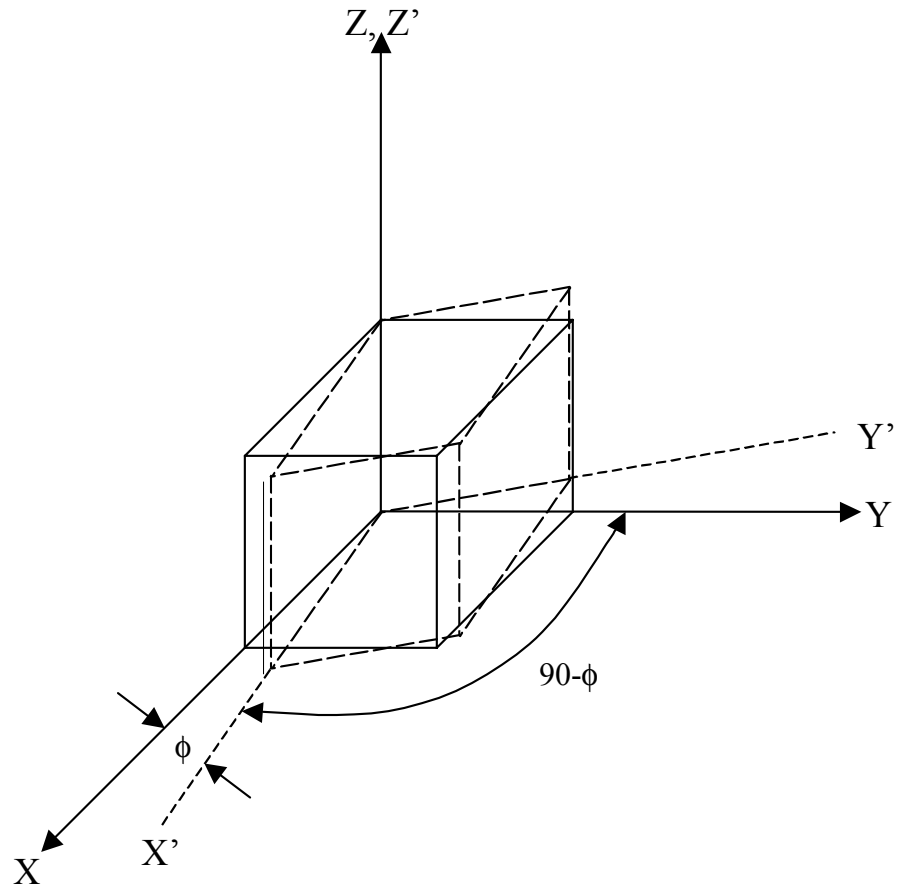


Figure 2.5. Schematic of two cubic lattices disorientated by angle ϕ about the z axis. The disorientation could be equally described by ϕ or $90-\phi$. The smaller angle is chosen by convention.

D. BACKGROUND ON MECHANICAL TESTING PROCEDURES FOR THE 978901 AND 978083 AA5083 MATERIALS

Taleff and Kulas [Ref. 21] conducted the mechanical testing of the 978901 and 978083 materials at the University of Texas at Austin. Tensile tests were conducted at temperatures of 425°C, 450°C, 475°C, and 500°C. At each temperature tests were conducted at the following true strain rates: $3 \times 10^{-5} \text{ s}^{-1}$, 10^{-4} s^{-1} , $3 \times 10^{-4} \text{ s}^{-1}$, 10^{-3} s^{-1} , $3 \times 10^{-3} \text{ s}^{-1}$, 10^{-2} s^{-1} , and $3 \times 10^{-2} \text{ s}^{-1}$. Prior to tensile loading, the samples were heated to the testing temperature and held there until the temperature stabilized. Stabilization generally occurred after 1 hour. Approximately constant true strain rate conditions were maintained by periodically adjusting the crosshead speed during testing as described in Tables 2.2 and 2.3. Samples for OIM analysis had been deformed to various intermediate strain values at strain rates of $3 \times 10^{-4} \text{ s}^{-1}$ and $3 \times 10^{-4} \text{ s}^{-2}$. These values of strain rate were chosen in order to study the strain rate response of the materials through the transition region.

l [in]	δl [in]	ϵ (%)	V [in/sec]	t [sec]
2.00	0	0	6.00e-4	833
2.50	0.5	25	7.50e-4	833
3.13	0.63	56.25	9.38e-4	833
3.91	0.78	95.31	1.17e-3	833
4.88	0.98	144.14	1.46e-3	833
6.10	1.22	205.17	1.83e-3	833

Table 2.2. Testing procedure to maintain approximately constant strain rate for materials 978901 and 978083 deformed in the superplastic regime; l is sample length, δl is change in length, ϵ is strain, V is cross-head velocity, and t is time.

l [in]	δl [in]	ϵ (%)	V [in/sec]	t [sec]
2.00	0	0	6.00e-2	8
2.50	0.50	25	7.50e-2	8
3.13	0.63	56.25	9.38e-2	8
3.91	0.78	95.31	1.17e-1	8
4.88	0.98	144.14	1.46e-1	8
6.10	1.22	205.18	1.83e-1	8

Table 2.3. Testing procedure to maintain approximately constant true strain rate for 978901 and 978083 materials deformed in the dislocation creep regime; l is sample length, δl is change in length, ϵ is strain, V is cross-head velocity, and t is time.

THIS PAGE INTENTIONALLY LEFT BLANK

III. EXPERIMENTAL PROCEDURES

A. OVERVIEW

In this investigation, AA5083 aluminum-magnesium alloys that had been processed for grain refinement and superplasticity were examined. Specifically, this study looked at AA5083 materials, designated 978083 and 978901, which had been provided by the University of Texas at Austin [Ref. 21], as well as proprietary SKY 5083 material that had been examined in previous work at the Naval Postgraduate School [Refs. 3-5].

The program for this investigation comprised three major phases. First, 978083 and 978901 materials were examined in the as-received condition; this initial part of the study revealed that the as-received materials had been supplied in a cold-rolled state. In the next phase, samples of as-received material were annealed for one hour at temperatures of 425°C, 450°C, 475°C, 500°C, and 535°C in order to examine the recrystallization behavior of each material throughout the temperature range for superplastic forming of these alloys. The highest annealing temperature, 535°C, was included to enable comparison to the earlier work on the SKY5083 material, which had been annealed and deformed at this temperature. In the final phase, microtexture methods were applied specifically to the study of the deformation mechanisms in the 978083, 978901 and SKY materials. This part of the investigation was conducted following elevated temperature strain under both superplastic and non-superplastic conditions. The principle method of microstructure and microtexture characterization was Orientation Imaging Microscopy (OIM). In addition, conventional optical microscopy was utilized to verify microstructures data obtained by the OIM method.

B. MATERIALS

Samples of the 978083 and 978901 materials were provided in the form of as-rolled sheet material. The as-rolled 978083 material was 1.4 mm in thickness while the 978901 material was 1.6 mm in thickness. The rolling direction was clearly identifiable from the surface texture on both of the materials. Compositions (in wt. pct.) of the 978083 and 978901 materials are provided in Table 3.1. From the Table 3.1, it is evident that the 978083 material generally contains a higher content of each alloying element. Based on thickness prior to the final rolling the cold reduction was calculated. The resulting cold reduction (%CW) is presented in Table 3.2.

Lot No.	Si	Fe	Cu	Mn	Mg	Cr	Zn	Ti	Zr
978083	0.09	0.21	0.04	0.86	4.71	0.10	0.05	0.01	0.00
978901	0.06	0.11	0.01	0.78	4.69	0.06	0.00	0.01	0.00

Table 3.1. Chemical composition data for the 978083 and 978901 materials (provided by the Texas Materials Institute of the University of Texas – Austin)

Lot No.	Gauge (mm)	% C.W.
978083	1.4	74.06
978901	1.6	73.97

Table 3.2. Final gauge after rolling and percent cold work for each material in the as-rolled condition; the 978083 was nearly twice as ductile as the 978901 material.

C. ANNEALING OF SAMPLES

The annealing of samples for the second phase of this study was performed in this laboratory. The 978083 and 978901 materials were annealed at 425°C, 450°C, 475°C, 500°C, and 535°C. The SKY material had been annealed at this latter temperature. A Ney model 2-160, Series II laboratory furnace was used for heating. A 12.7 mm thick brass plate was placed on the hearth to aid in temperature stabilization and the furnace was then allowed to equilibrate at the desired annealing temperature. Temperature measurement was obtained by averaging the reading two chromel-alumel thermocouples. The thermocouples were placed on either side of the samples. Measurements showed that the temperatures stabilized within 0.5° C of the desired value within two minutes. After one hour of total elapsed time, the samples were removed and allowed to cool in air to room temperature. At no time during annealing did the average temperature indicated by the two thermocouples exceed 1.0°C variance from the desired annealing temperature.

D. SAMPLE PREPARATION FOR OIM

In Orientation Imaging Microscopy on aluminum alloys, the region from which the electron backscatter diffraction are formed extends only to a depth of 50 nm below the surface [Ref. 19]. Consequently, extreme care must be exercised in sample preparation to achieve a uniform, smooth surface with a minimum of damage due to metallographic preparation. Careful handling and storing of the specimen is also essential due to the sensitivity of the technique to surface contamination and the presence of oxide layers.

Accordingly, samples were sectioned from the sheet material using a Buehler low-speed saw equipped with a diamond-wafering blade. Samples in the as-received condition were sectioned parallel to the rolling direction to facilitate examination of the effects of rolling in the RD-ND plane, as illustrated in Figure 3.1. Samples that had been deformed at elevated temperature were sectioned as illustrated in Figure 3.2. Again, these samples were examined in a plane corresponding to the RD-ND plane of the as-received condition of the material.

Mechanical grinding and polishing of the samples was accomplished as summarized in Table 3.3. Initial grinding was carried out using successively finer silicon

carbide fixed abrasives. The silicon carbide papers were placed on a flat surface and lubricated using distilled water. Using only minimal downward force, grinding was conducted in one direction until evidence of the prior grinding step was removed. The sample was then rotated 90° and the procedure was repeated on the next grit. Between each grinding the samples were flushed with distilled water. Rotating wheels were used for subsequent polishing steps using oil-based diamond suspensions and a final mechanical polishing step used a colloidal silica suspension. Distilled water was used to dilute the colloidal silica suspension and provide additional lubricant. Care must be taken to use dilute dispersions of all abrasives and thus avoid saturation of the polishing wheels with the abrasive materials. Excessive use of the polishing media can result in contamination of the sample's surface. Also, minimization of downward pressure during polishing is essential. Too much downward force can result in superficial deformation on the sample by displacing the lubricants in the abrasive solutions. After each of these polishing steps, ultrasonic cleaning was performed for ten minutes in either ethanol or methanol.

A distortion-free final polish was required in order to obtain the most distinct diffraction patterns. To achieve this, a final electro-polishing step was conducted with the Buehler Electromet 4 Electropolisher using a 20% Perchloric Acid – 80% Ethanol electrolyte solution. Prior to use the solution was cooled to -25°C. Samples were then either placed directly in the scanning electron microscope or stored temporarily in ethanol or methanol to prevent surface oxidation while awaiting examination.

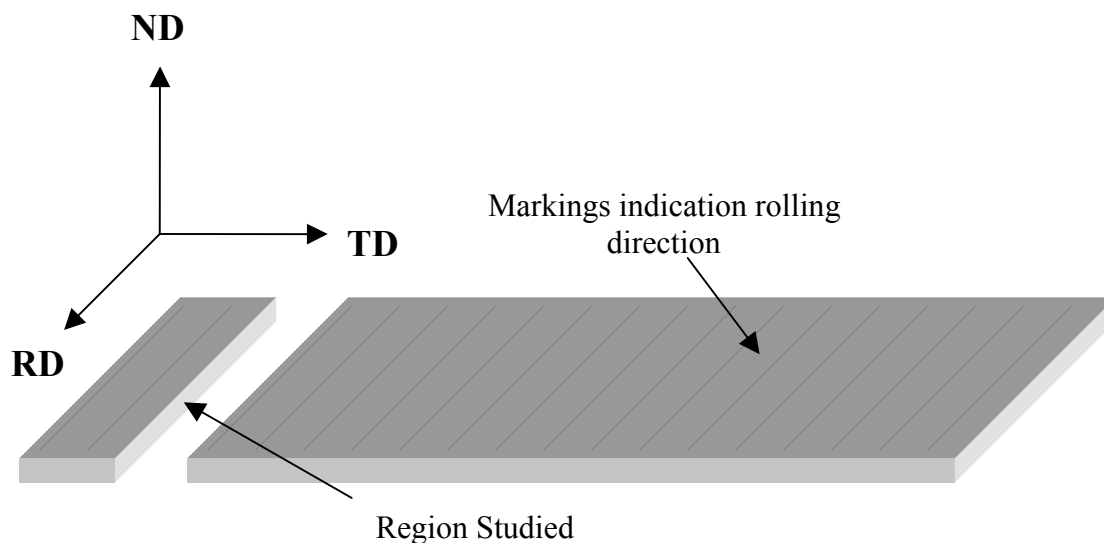


Figure 3.1. Schematic of material in as-rolled condition. RD, ND, and TD labels on the axis represent rolling direction, normal direction, and transverse direction respectively. The sample was sectioned along RD in order to examine the microstructural properties induced by rolling.

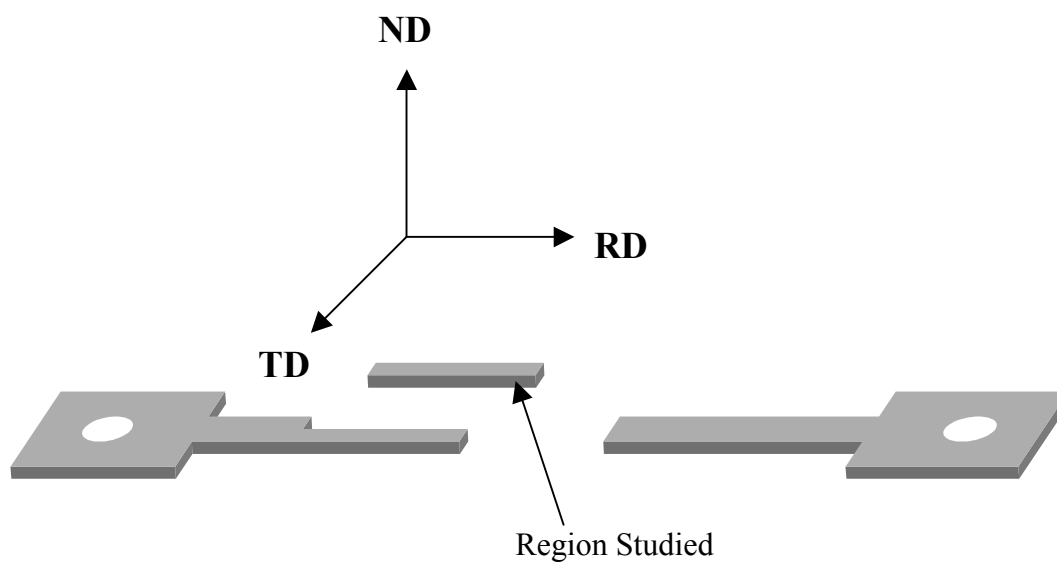


Figure 3.2. Schematic of deformed sample illustrating sectioning for OIM examination.

Step	Abrasive	Time	RPM
1	500 Grit SiC Paper	30 sec	n/a
2	1000 Grit SiC Paper	30 sec	n/a
3	2400 Grit SiC Paper	30 sec	n/a
4	4000 Grit SiC Paper	30 sec	n/a
5	3 μm Metadi Diamond Suspension	10 min	180
6	1 μm Metadi Diamond Suspension	10 min	180
7	0.05 Colliodal Silica	10 min	120

Table 3.3. Mechanical Polishing

E. ELECTRON BACKSCATTER DIFFRACTION PATTERN COLLECTION

Electron backscatter diffraction patterns were obtained in a TOPCON SM-510 Scanning Electron Microscope (SEM) equipped with a tungsten filament. The microscope was operated at an accelerating potential of 20 kV. The polished sample was mounted in the SEM on a specially designed stage that holds the sample at a 70° angle relative to the incident electron beam, enabling Bragg Diffraction conditions to be met without having to rock the electron source. When an electron beam strikes a surface inclined in this manner, the electrons penetrate the sample surface and are diffracted to produce distinct patterns based on the local lattice orientation. These patterns appear as multiple intersecting lines, termed Kikuchi bands. The arrangement of the bands can be used to index the pattern and obtain an unambiguous lattice orientation if the patterns arise from a single crystal, or within one grain of a polycrystal.

The diffracted electrons illuminate a phosphor screen mounted near the sample. A low-light camera is used to collect the image of the Kikuchi patterns from the phosphor screen for indexing by the OIM software. The arrangement of this equipment is illustrated in the simplified schematic in Figure 3.3. The image collected by the low-light camera is subsequently processed to remove noise and enhance contrast. After averaging over eight frames the image of the Kikuchi pattern is indexed by computer. Figure 3.4(a) shows a processed backscatter diffraction pattern prior to indexing.

The OIM software compares the processed backscatter diffraction pattern to a set of reference patterns. These reference patterns are comprised of intersecting lines that the computer attempts to match to the Kikuchi bands displayed in the backscatter pattern. The shapes of the intersecting lines on the reference patterns are determined by the Bravais lattice and lattice dimensions (lattice parameter) of the material under study. Prior to the collection of data, the user must instruct the software to calibrate reference patterns to a sample Kikuchi pattern from the material. This calibration corrects for distance errors caused by slight mounting variations from one sample to the next that would otherwise cause the lines in the reference pattern to be of different length than those generated by the diffraction pattern. For a given diffraction pattern there are generally several possible reference patterns that can be fit to the Kikuchi bands. Each

reasonable solution is assigned a numerical rank using a voting scheme based on how closely the proposed reference pattern fits the Kikuchi bands. The reference pattern that represents the best fit to the Kikuchi bands is taken as the orientation of the point and the software records the Euler angles for that pattern. Figure 3.4 (b) shows the superposition of a proper solution on the backscatter diffraction pattern of Figure 3.4(a). The solution is expressed in terms of the Euler angles φ_1 , Φ , and φ_2 (Bunge's definition [Ref. 20]) that describe the rotation necessary to cause the cube axes and sample axes to coincide.

The OIM software also computes two figures of merit for the diffraction data: the confidence index (CI) and the image quality (IQ). The CI is a measure the software's certainty that it has selected the correct orientation for the data point. Its value is based on the voting scheme used in ranking proposed solutions and is determined by the equation $CI = (V_1 - V_2) / V_{ideal}$ where V_1 is the number of votes for the first solution and V_2 is the number of votes for the second solution. Finally, V_{ideal} is the total number of votes for all proposed solutions. Essentially, CI is a measure of the difference between the number of votes for the best solution and for the second best solution. If the difference is large, the software has indicated that the best solution is highly likely and the assigned CI is therefore high. If the difference is small, there is uncertainty in the software solution and the CI will be low. The CI can range from zero to one and CI values greater than 0.1 correspond to a 95% probability that a Kikuchi pattern has been correctly indexed.

The IQ is a measure of the sharpness of a given electron backscatter diffraction pattern. While the IQ can be adversely affected by conditions at the sample surface it is also a measure of the perfection of the crystal lattice, and this is of primary concern here. Distortions in the crystal lattice caused by imperfections such as dislocations, or the overlapping and spreading of patterns nearby grain boundaries, produce more diffuse patterns and more poorly defined Kikuchi bands. This means that image quality can be used to give a qualitative description of regions of high strain energy and high dislocation density. Regions of low IQ are also found nearby grain boundaries.

The electron beam provided by a SEM has a typical diameter of about 0.15 μm , i.e. 150 nm. Therefore, the beam only interacts with a very small volume of the sample relative to typical grain dimensions in engineering materials and so the resulting

orientation data represents the local lattice orientation at a point within the grain. If the electron beam is displaced from point to point in a pattern on the surface of a sample, the resulting orientation data may be assembled into a map of orientations of the sample surface.

The OIM software displaces the electron beam in a raster pattern across the sample surface. In this investigation, a hexagonal pattern was used for all samples. A typical scan pattern is shown in Figure 3.5. The size of the scan and the step size are user selectable. The system employed in this study was capable of indexing about 3 points per second, or 10,000 points per hour. The region to be scanned is selected on a secondary electron image of the surface. As the surface of the sample is scanned, data for each point is saved in a single line comprising the Euler angles (ϕ_1 , Φ , ϕ_2), coordinates relative to the origin of the scanned region (x,y), the IQ, and the CI. Phase identification is also saved but was not used in this investigation due to the inability to distinguish very small second phase Al_6Mn particles from the aluminum matrix. It is worth noting that the diffraction pattern image of Figure 3.3 is not saved. The set of data lines corresponding to each point in a scanned region on the sample surface is save in a .ang file. This file is the source for all subsequent data analysis.

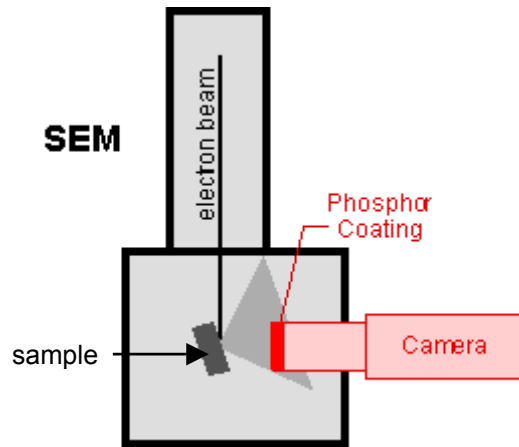
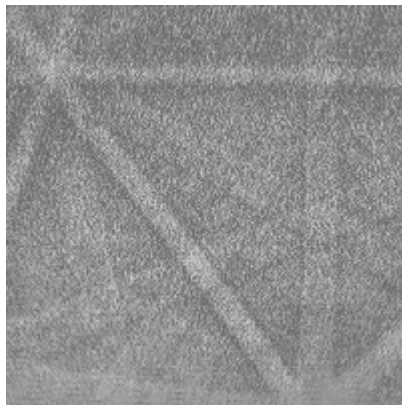
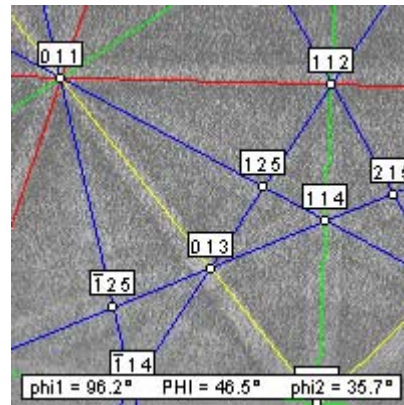


Figure 3.3. Schematic [From TEXSEM] of the set-up of the SEM for OIM. The sample is tilted in order to meet Bragg Diffraction conditions. The Phosphor screen collects diffraction patterns.



(a)



(b)

Figure 3.4. Electron backscatter diffraction patterns illustrating appearance of Kikuchi patterns. (a) Processed pattern prior to indexing and (b) after indexing. The colored lines in (b) are the reference pattern.

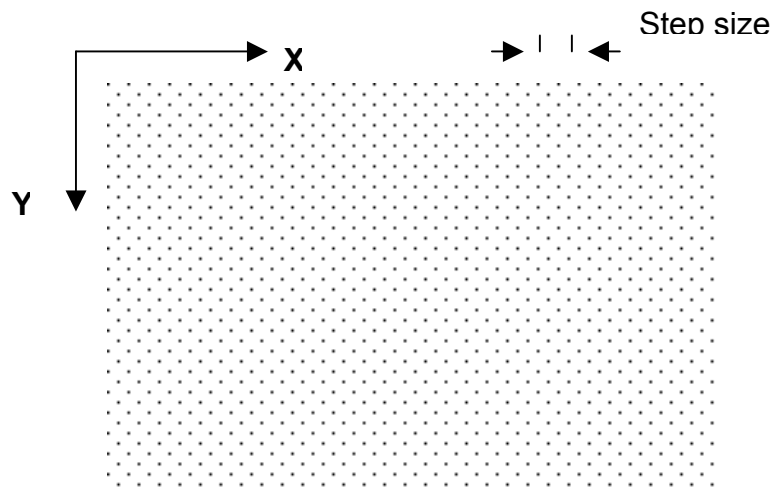


Figure 3.5. A typical hexagonal raster scan of a sample surface illustrating OIM coordinate system and step size.

F. ORIENTATION IMAGING MICROSCOPY ANALYSIS

There are several distinct methods for depicting the orientation data in OIM. In this study, the discrete pole figure was employed extensively. The pole figure is a two-dimensional stereographic projection of a set of poles relative to RD, TD and ND. Pole figures are especially useful in evaluating preferred orientation, or texture. An example of a pole figure for a single orientation data point is shown in Figure 3.6

OIM is also capable of assembling the orientation data into grain maps. It is important to recognize the importance in these maps of the grain tolerance angle, which defines the maximum disorientation between two points that are considered to reside in the same grain. In general, a grain tolerance angle of two degrees was used in this work. If two adjacent points have a disorientation angle of greater than two degrees, it is assumed that a grain boundary exists and that the points belong to separate grains. The OIM Analysis software creates a grain map by considering the orientations of all points in a scan, and then uses orientation or other attributes to develop contrast corresponding to the region of the map. Figure 3.7(a) illustrates how the OIM software recognizes grain structure by comparing orientation. The representation shown in Figure 3.7(a) is termed a unique grain color map. In order to make it easier to visualize the grain structure, the software assigns colors randomly to each grain. The color assigned is not related to the properties of the grain, and grains that are depicted by the same color may or may not have anything in common. The format of the unique grain color map is analogous to a geographical map in which color is only used to help distinguish political boundaries.

Grain maps can also incorporate additional information if desired. The software is capable of including a grayscale — the darkness of a region being proportional to a selected property. In this work, IQ is typically represented by a grayscale. Figure 3.7(b) illustrates this effect. By indicating IQ using a grayscale, regions such as grain boundaries and other regions of high dislocation density appear darker. Using IQ grayscale alone would be an alternative method of visualizing grain structure. While unique grain color maps determine grain boundaries by point-to-point disorientations, IQ grayscale maps indicate grain boundaries purely by the quality of the diffraction pattern.

OIM software is capable of superimposing showing both representations simultaneously. An example is shown in Figure 3.7(c).

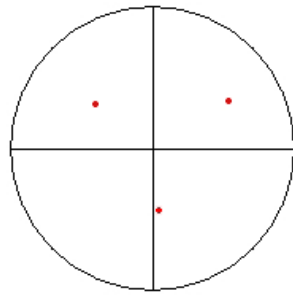
OIM software also provides the ability to relate pole figure data directly to grain maps. By using the highlighting feature, one can highlight a point on a pole figure and the corresponding grains will be highlighted on the grain map in the same color. Using this feature, one may show how preferred textures are distributed with respect to grain structure. Figure 3.7(d) shows an example of this type of highlighting.

OIM software has the ability to calculate grain size distributions and average grain sizes, both based on the unique grain color map. The diameter of a grain is determined by first counting the number of points in a grain and multiplying that by a scaling factor based on the step size and pattern of the raster. The grain shape is then approximated as a circle and the diameter is calculated based on that circle. When determining an average grain diameter, grains that touch an edge of the map are discarded.

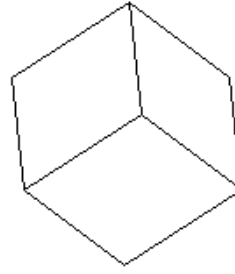
Another useful feature of the OIM software is the ability to calculate the disorientation angle between grains and represent this data in the form of a histogram or on a grain map by color-coding ranges of disorientation angle. Histograms are useful in determining the nature of the distribution by comparing it to the disorientation distribution for randomly oriented cubes, as determined by Mackenzie [Ref. 22].

Clean-up procedures in the OIM analysis software were applied to all scans in order to compensate for erroneous data points. While pattern indexing in OIM is generally quite effective in most regions of a sample surface, the system does have difficulty indexing in some circumstances. Examples are regions of low image quality where Kikuchi bands are diffuse, or nearby grain boundaries where patterns from adjacent grains can superimpose. In general, clean-up methods correct for small grains of low CI by incorporating them into larger adjacent grains of high CI. Three clean-up methods were used for each scan. First, CI Grain Standardization assigned the highest CI for a point within a grain to the entire grain. Then, Neighbor CI Correlation assigned a grain with a confidence index less than 0.1 (95% certainty) to the neighboring grain with

the highest CI. Finally, Grain Dilation assigned any leftover grains with a grain size corresponding to one data point to its neighbor with the highest CI.

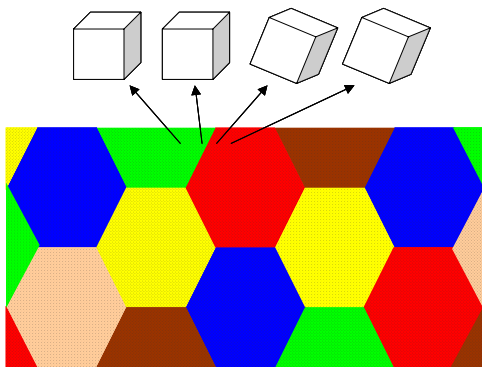


(a)

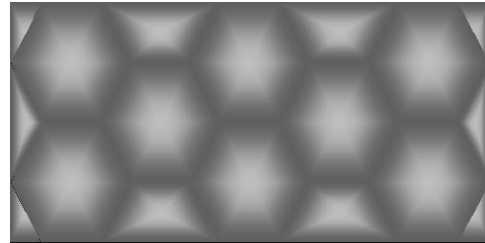


(b)

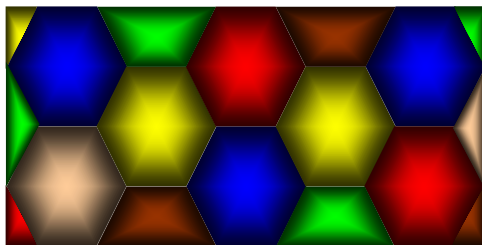
Figure 3.6 (a) Sample $\{100\}$ pole figure representation of the crystallographic orientation show in (b).



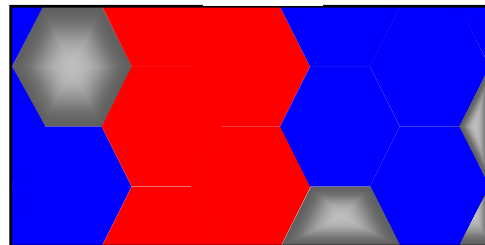
(a)



(b)



(c)



(d)

Figure 3.7 OIM grain map representations. (a) Unique grain color map derived from orientation data. Dots represent data points. Cubes illustrate how grain boundary between green and red grains is based on change in orientation. (b) IQ grayscale map. Grain boundaries appear dark because they are regions of high lattice imperfection at therefore result in more diffuse, lower quality patterns. (c) Illustrates ability to superimpose Unique Grain Color Maps and IQ grayscale map. (d) Is an IQ grayscale map that reflects highlighting of orientations on a corresponding pole figure.

G. OPTICAL MICROSCOPY

Optical microscopy was used in order to provide comparison with grain structures obtained in OIM. Samples were mounted and prepared in the same fashion as described in Section 3B. After electropolishing, the samples were electrolytically etched using the etching attachment to the Buehler Electromet 4 apparatus. The electrolyte was Barker's reagent, which consists of 2% HBF_4 and 98% water. The samples were electrolytically etched at 1 volt for 30 seconds and examined in a Zeiss Jenaphot optical microscope using plane-polarized light. Images were examined using crossed polars and acquired in polarized light.

IV. RESULTS AND DISCUSSION

A. THE AS-RECEIVED CONDITION OF THE 978901 AND 978083 AA5083 ALLOY MATERIALS

The microstructures of the as-received 978083 and 978901 materials are essentially the same and reflect severe deformation resulting from the cold working during the final stage of the deformation processing. A unique grain color image of the as-received 978901 material is shown in Figure 4.1, and of the as-received 978083 material in Figure 4.2. In both cases, a grayscale reflecting image quality has been superimposed on the unique grain color data. These data reflect a mixture of very fine (sub)grains and better-defined and somewhat coarser grains that are elongated in the direction of rolling. In the images of Figures 4.1 and 4.2, a darker grayscale corresponds to lower the image quality. The regions of low image quality may be attributed to regions of high dislocation density resulting from high strain in the crystal lattice resulting from cold work in the presence of dispersed Al_6Mn particles. In some locations the low image quality also appears to delineate regions nearby grain boundaries.

The microstructure of the 978083 material obtained from optical microscopy is shown in Figure 4.3. The image was obtained at a relatively high magnification of 1500 diameters although it is at a lower effective magnification than the OIM images in Figures 4.1 and 4.2. The grain structure is essentially that of a cold-worked material, thus helping to validate the OIM data.

The orientation data for the 978901 material are plotted in Figure 4.4 in the form of a contour plot in the fundamental zone of Euler space for a face centered cubic material. The contours were calculated in software by smoothing of Gaussian distributions about locations in Euler space of the discrete orientation measurements. Data for the 978083 material were essentially the same as those for 978901 and are not presented here. These data clearly show a predominant B (or brass) texture component; the ideal B orientation is $\{110\}\langle 112 \rangle$, where this notation refers to $\{\text{plane parallel to the rolling plane}\}\langle \text{direction parallel to the rolling direction} \rangle$. This component has two crystallographically distinct variants, B_1 and B_2 , which are located at $\varphi_1 = 35^\circ$, $\Phi = 45^\circ$,

and $\varphi_2 = 0^\circ$; and $\varphi_1 = 55^\circ$, $\Phi = 90^\circ$, and $\varphi_2 = 45^\circ$, respectively. These variants are readily distinguished in electron backscatter diffraction analysis and so the relative intensities at the locations for the two variants are not the same if the relative volume of material having each of these orientations differs in the region under investigation. Examination of Figure 4.3 shows that the local intensity is greatest at the exact B orientation and that most orientations lie within about 15° of the B orientation. Figure 4.4(a) shows discrete pole figures corresponding to the data of Figures 4.1 and 4.3; the presence of the B texture is readily apparent in the concentration of orientations near the center of the $\{220\}$ diagram. These texture data are consistent with a heavily cold worked condition in the as-received material.

The highlighting features in the OIM software permits the correlation of orientations in the pole figures to the spatial distribution of these orientations on the grain maps. This is accomplished by selecting an orientation of interest on the pole figure. The software highlights all points within a specified tolerance of the selected point and highlights the associated grains in the same color. Thus, the spatial distribution of the two texture components, B_1 and B_2 , is shown in Figure 4.5(b). The grain map now shows that the microstructure comprises bands of lattice orientation that alternate between the orientations of the B_1 and B_2 texture variants; this is reflected in the alternating red and blue color bands on the grain map. The appearance of these bands is consistent with the deformation-banding model of severe rolling operations [Refs. 23-29] and has been previously documented using OIM by Swisher [Ref. 30].

The highlighting features in the OIM software may also be employed to highlight the locations of the interfaces between grains in the microstructure. A histogram of the grain-to-grain disorientation angles is shown in Figure 4.5(c); the high-angle boundaries (55° - 62.8°) are also highlighted on the grain map of Figure 4.5(b) wherein it is seen that the high-angle boundaries tend to separate the texture variants. The low-angle boundaries (2° - 15°) correspond to a cell structure within the bands. Figure 4.6 provides a similar analysis of the as-received condition of the 978083 material. Comparison of these data to corresponding data in Figure 4.5 reveals the same B-type texture and regions of lattice orientation that alternate between the B_1 and B_2 variant orientations. Again, the high-angle boundaries separate the variants while low-angle

boundaries are involved in a cellular structure within the variants. The band-like arrangement of the variants is less apparent in the region of the 978083 material represented in Figure 4.6 than was apparent in the 970901 material (Figure 4.5).

These high-angle interfaces may become nucleation sites for recrystallization during annealing after deformation processing, although the origin of the recrystallized grains during annealing of deformed metals remains an active area of investigation [Ref. 14]. As discussed in Chapter II, superplastic behavior requires a fine, equiaxed grain structure with high-angle boundaries that can support grain boundary sliding. Such a microstructure may be achieved if sufficient particles of the Al_6Mn are present in the rolled condition in order to serve as sites for particle-stimulated nucleation of recrystallization [Ref. 17].

The low-angle boundaries, which were highlighted in Figures 4.5(d) and 4.6(d), are generally contained within the band-like structures. This indicates the presence of a cell-like sub-structure within the bands. The distribution of these low angle boundaries within the bands accounts for the spread in orientations in the pole figures.

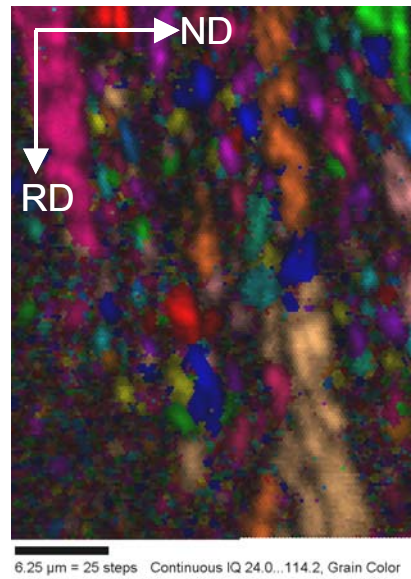


Figure 4.1. Unique grain color maps with image quality grayscale of a $20\mu\text{m} \times 30\mu\text{m}$ area of 978901 material in the as received condition. Step size is $0.2\mu\text{m}$. Grayscale represents image quality with darker regions indicative of lower image quality. Data reflects a mixture of very fine (sub)grains and better-defined and somewhat coarser grains that are elongated in the direction of rolling. The regions of low image quality may be attributed to regions of high dislocation density resulting from high strain in the crystal lattice resulting from cold work in the presence of dispersed Al_6Mn particles. In some locations the low image quality also appears to delineate regions nearby grain boundaries.

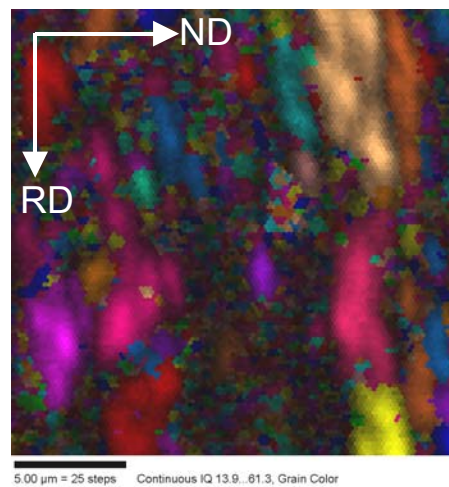


Figure 4.2. Unique grain color maps with image quality grayscale of a $20\mu\text{m} \times 20\mu\text{m}$ area of 978083 material in the rolled condition. Step size is $0.25\mu\text{m}$. Image Quality grayscale. This structure exhibits essentially the same attributes as 978901 material described in Figure 4.1.

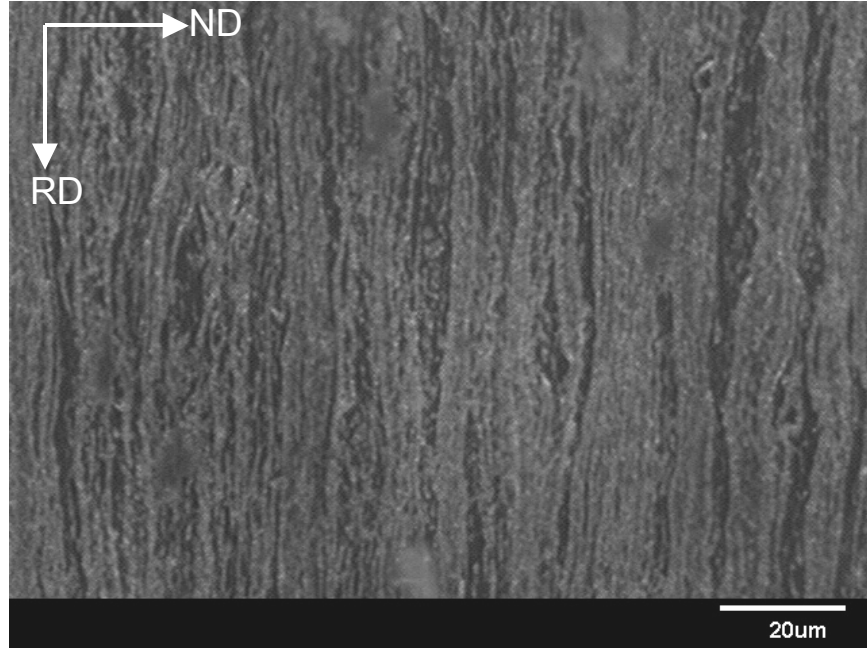


Figure 4.3. Optical micrograph of as-received 978083 material. Image acquired at 1500X magnification. The microstructure is essentially that of a cold-worked material.

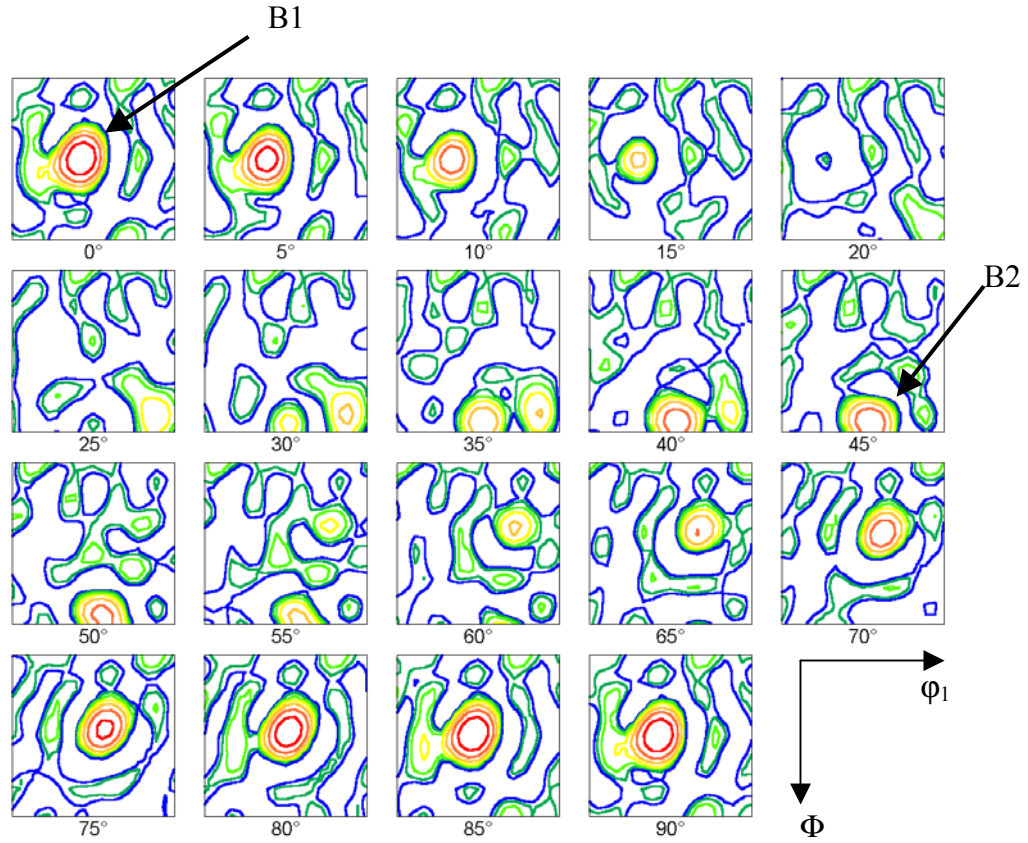


Figure 4.4. Contour map in Euler space for the 978901 material. Red lines indicate regions of higher orientation concentration while blue lines correspond to random concentration. A predominant B (or brass) texture component is present and has two crystallographically distinct variants, B₁ and B₂, which are located at $\phi_1 = 35^\circ$, $\Phi = 45^\circ$, and $\phi_2 = 0^\circ$; and $\phi_1 = 55^\circ$, $\Phi = 90^\circ$, and $\phi_2 = 45^\circ$, respectively

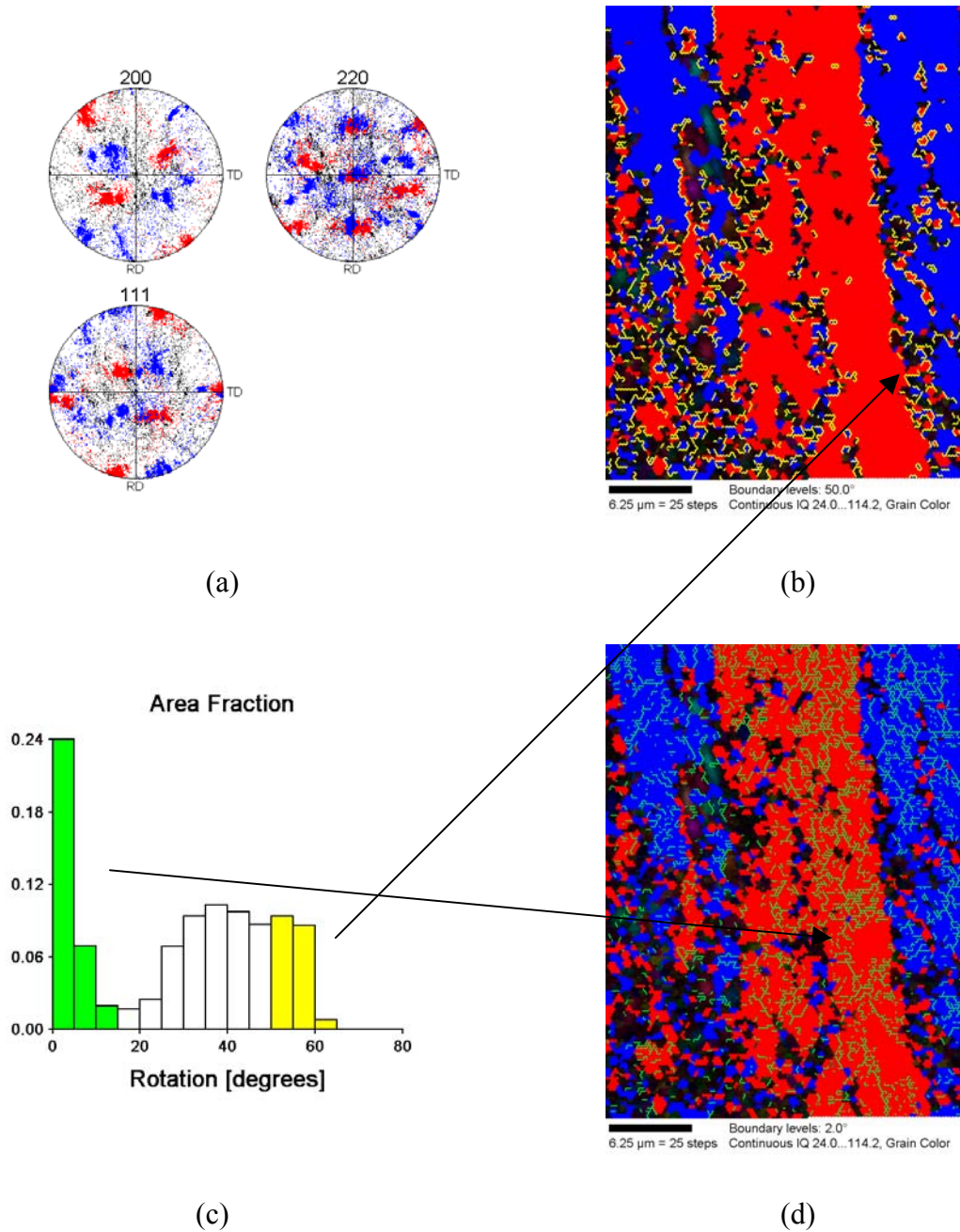


Figure 4.5. OIM Analysis of 978901 material in the as received condition. The pole figures (a) reveal a brass texture. The B1 and B2 components have been highlighted using a 15° tolerance. The result is alternating band texture evident in (b) and (d). Maps (b) and (d) have also been highlighted to reflect high and low angle boundaries of the disorientation histogram (c). High angle boundaries tend to encircle the band-like structure. Low angle boundaries (d) tend to fall within the band-like structures, indicating the presence of a sub-structure within the bands.

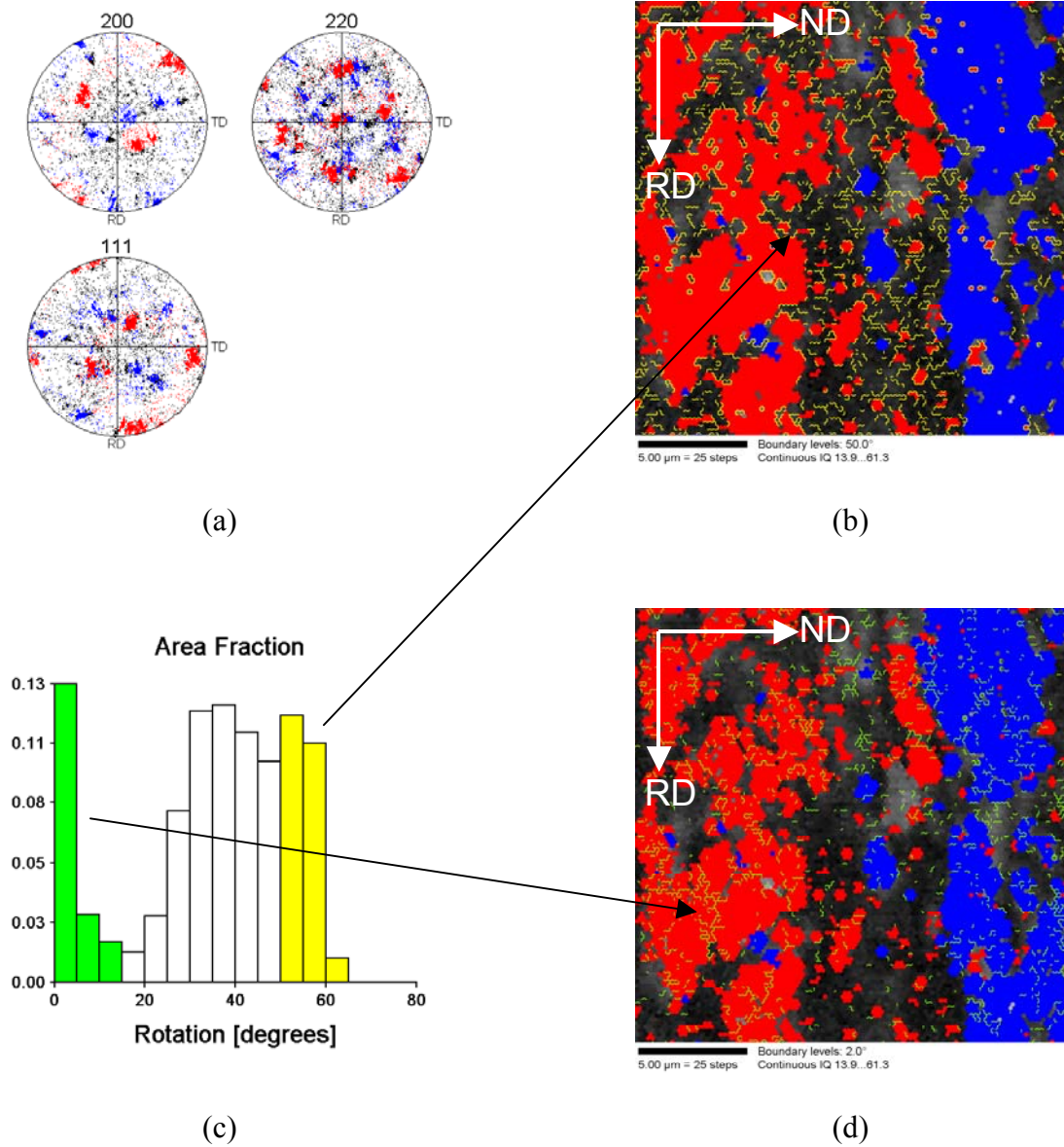


Figure 4.6. OIM Analysis of 978083 material in the as rolled condition. The pole figures (a) reveal the same brass texture and has been highlighted using a 15 degree tolerance to reflect the alternating band texture evident in (b) and (d). Maps (b) and (d) have also been highlighted to reflect high and low angle boundaries of the disorientation histogram (c). The band-like arrangement is present, but is weaker than in the 978901 material (Figure 4.5).

B. EFFECT OF ANNEALING ON THE 978901 AND 978083 MATERIALS

Samples of both the 978901 and the 978083 materials were annealed for 1 hour at 425°C, 450°C, 475°C, 500°C or 535°C, as described in Chapter III. Unique grain color maps corresponding to each of these annealing temperatures are provided in Figure 4.7 for the 978083 material and in Figure 4.8 for the 978901 material. Image quality has been superimposed in both cases. An optical micrograph of 978901 material annealed at 500°C is provided in Figure 4.9. Altogether, these data indicate that both materials respond in essentially the same way to these annealing treatments, although recrystallization may be incomplete in the 978901 material following the 425°C anneal. Otherwise, the rolled microstructure has been replaced by a fine, equiaxed grain structure that should be capable of supporting superplastic response. Optical results confirm the conclusions from OIM.

Increased annealing temperature up to 500°C apparently results in only minimal grain coarsening, while annealing at 535°C appears to result in a coarser grain size. The influence of annealing temperature on grain size is documented in Figure 4.10 and in Table 4.1. The grain size values are area-weighted average grain diameters corresponding to an average of four 100 μm x 100 μm area OIM scans using a step size of 1.0 μm for each annealing condition. The grain size data are obtained by calculation the equivalent area of one pixel in the image and then multiplying this value by the number of pixels in each grain. The equivalent diameter of each grain is then determined by assuming a circular grain shape. The average grain diameter varies from about 6.0 μm to about 8.0 μm as the annealing temperature increases from 425°C up to 500°C. Above 500°C both materials show a more distinct increase in grain size as a function of annealing temperature, and the 978901 material appears to show a slightly greater rate of coarsening than the 978083 material. This suggests that superplastic forming temperatures of 500°C or below will result in a finer as-formed grain size for these materials.

Both materials show an abundance of high angle boundaries following annealing at all temperatures. Figures 4.11 and 4.12 show histograms representing the distributions of the grain-to-grain disorientation angles for the 978901 and 978083 materials,

respectively. For both materials the histogram shape closely resembles the Mackenzie distribution [Ref. 22] for the disorientations of cubes of random orientation. The data of Figures 4.11 and 4.12 show that $\geq 90\%$ of the boundaries have disorientation angles $\geq 15^\circ$, except for the 978901 material annealed at 425°C . As noted earlier, recrystallization is apparently incomplete for this material and temperature combination, and this is reflected here in the retention of recovered substructure.

As noted in Chapter II, high-angle boundaries are necessary because they slide more readily than low-angle boundaries. An equiaxed grain shape also facilitates grain boundary sliding. In Figure 4.13, the data of Figures 4.7(d) and 4.8(d) have been re-plotted to show only the grain boundaries with disorientations $\geq 15^\circ$. Figure 4.13(a) is for the 978901 material, and Figure 4.13(b) is for the 978083 material. From these data, it is evident that the grain boundaries of disorientation $\geq 15^\circ$ surround equiaxed grains in both materials. Thus, these microstructures are essentially equivalent in meeting the requirements of a fine, equiaxed grain structure with grain boundaries capable of supporting GBS.

The B-type deformation texture observed in both of the as-received materials is replaced by a recrystallization texture following annealing for all annealing temperatures. Microtexture data is shown for the 978901 material in Figure 4.14 and for the 978083 material in Figure 4.15. Both materials exhibit a predominant random texture component although a weak cube-type texture component ($\langle 001 \rangle \{uv0\}$) is also apparent in all of the discrete pole figures in Figures 4.14 and 4.15. The cube-type component is most readily apparent in the $\{200\}$ pole figures in the concentration of orientations near the center of the pole figures. The random component is consistent with particle-stimulated nucleation [Ref. 31] of recrystallization associated with dispersed Al_6Mn particles in the microstructure. Such a random texture results in a predominance of high-angle boundaries and thus promotes grain boundary sliding and superplastic deformation.

The weak cube-type component reflects a tendency of the $\{100\}$ to align with the rolling plane although no low-index direction, such as $\langle 100 \rangle$, appears to align with the rolling direction. A schematic of this circumstance is shown in Figure 4.16; this component will be shown to become more distinct during elevated temperature

deformation for some deformation conditions. The cube-type component is most likely related to the initiation of recrystallization at prior grain boundaries, interfaces between deformation bands or other features other than the Al_6Mn particles. Thus, both particle stimulated and grain boundary nucleation mechanisms contribute to the formation of the annealed microstructures in these materials. The random grain orientations associated with PSN result in random, high-angle boundaries and so tend to favor GBS. Alteration of processing to reduce or eliminate the cube component may result in materials of greater superplastic ductility.

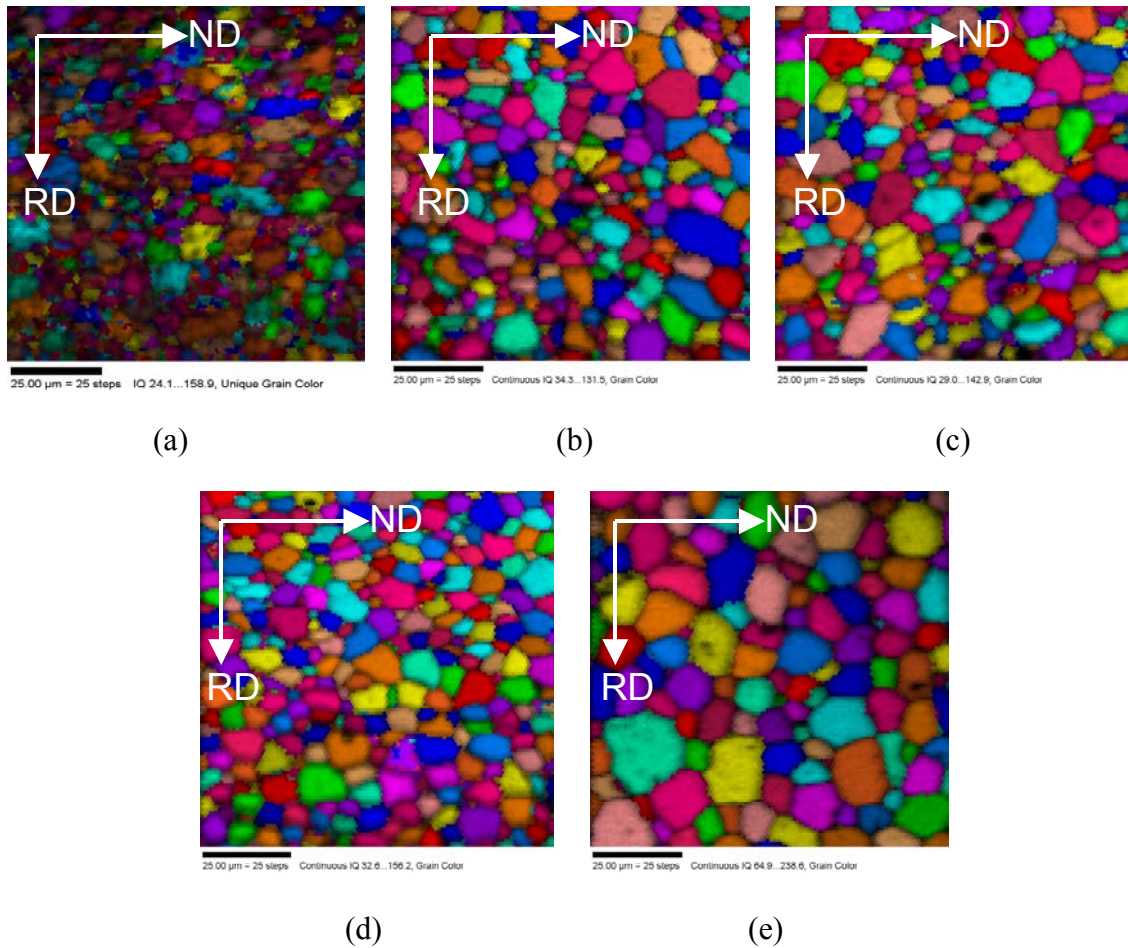


Figure 4.7. Unique grain color maps with image quality grayscale of 978901 material annealed for 1 hour at the following temperatures: (a) 425°C, (b) 450°C, (c) 475°C, (d) 500°C, and (e) 535 °C. All scans are 100 μm x 100 μm with a 1μm step size. At 425 °C (a), the microstructure is not fully recrystallized. At all other temperatures, the microstructure consists of fine, equiaxed grains. Annealing up to 500 °C (d), results in only minimal increases in grain size while annealing at 535° C (e) results in greater coarsening. Subsequent stress-strain testing was performed at 500°C

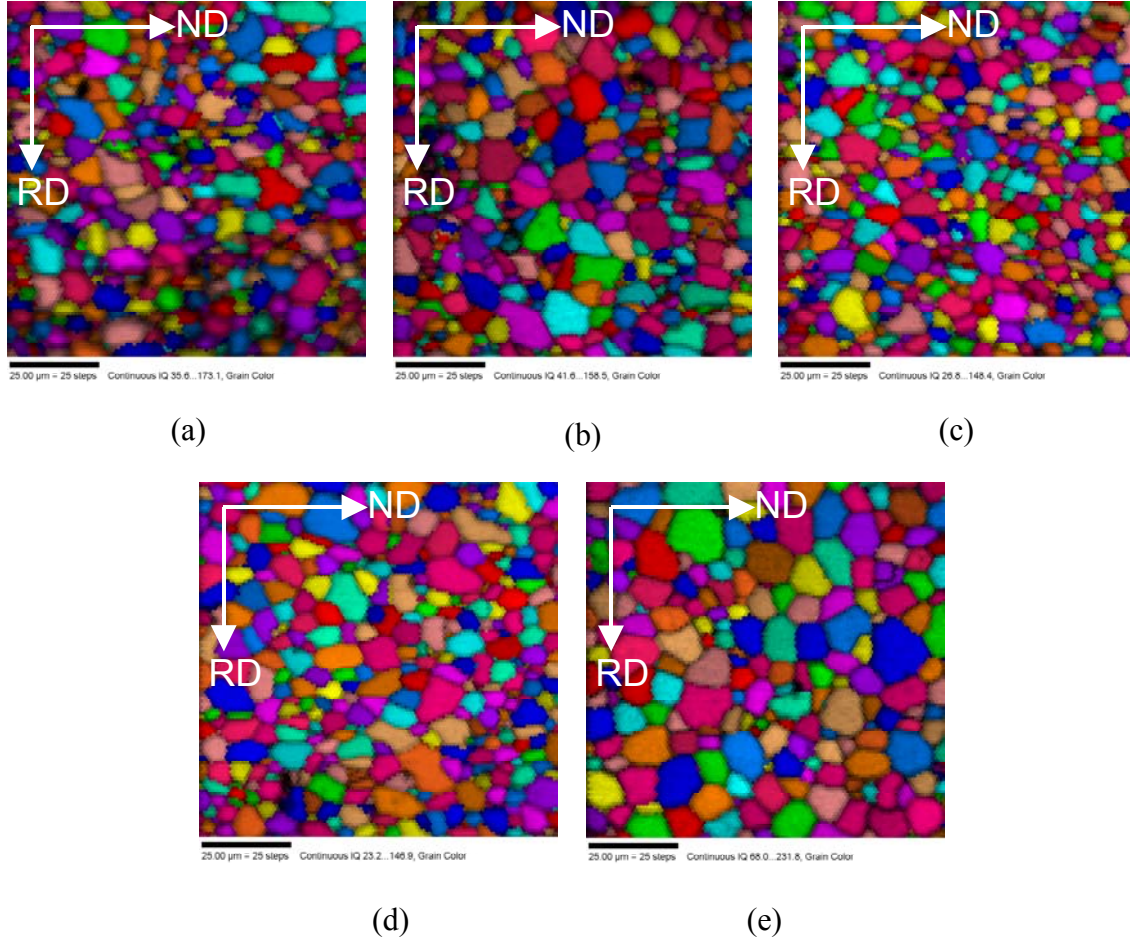


Figure 4.8. Unique grain color maps with image quality grayscale 978083 annealed for 1 hour at the following temperatures: (a) 425°C, (b) 450°C, (c) 475°C, (d) 500°C, and (e) 535°C. All scans are 100 μm x 100 μm with a 1 μm step size. This material exhibits a fine equiaxed structure at all annealing temperature. Like 978901 material, Figure 4.6, this material shows greater coarsening at 535 °C (e). All subsequent stress-strain testing was conducted at 500°C(d).

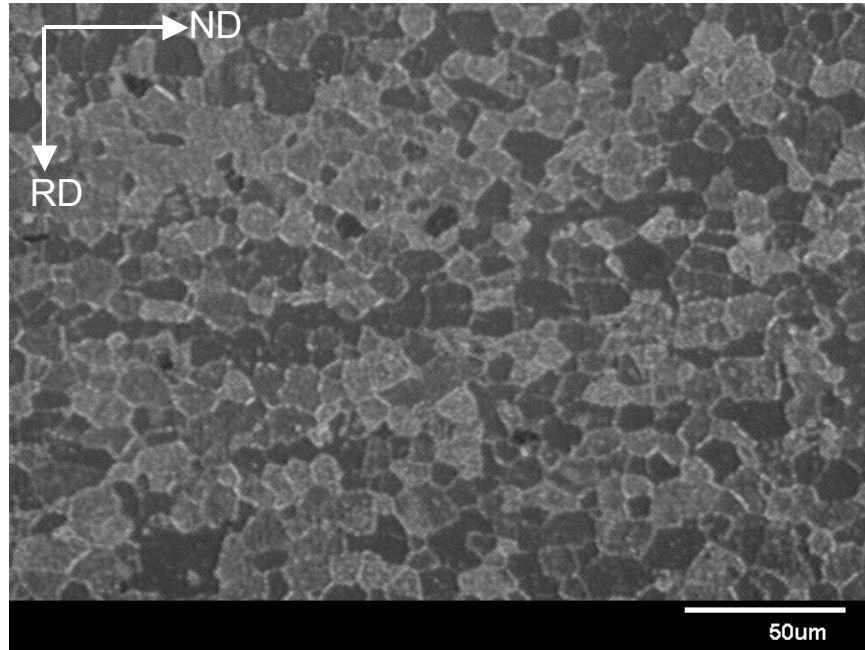


Figure 4.9. Optical micrograph of 978901 material annealed at 500°C. Image taken at 750X magnification. The microstructure is essentially the same as Figures 4.7(d)

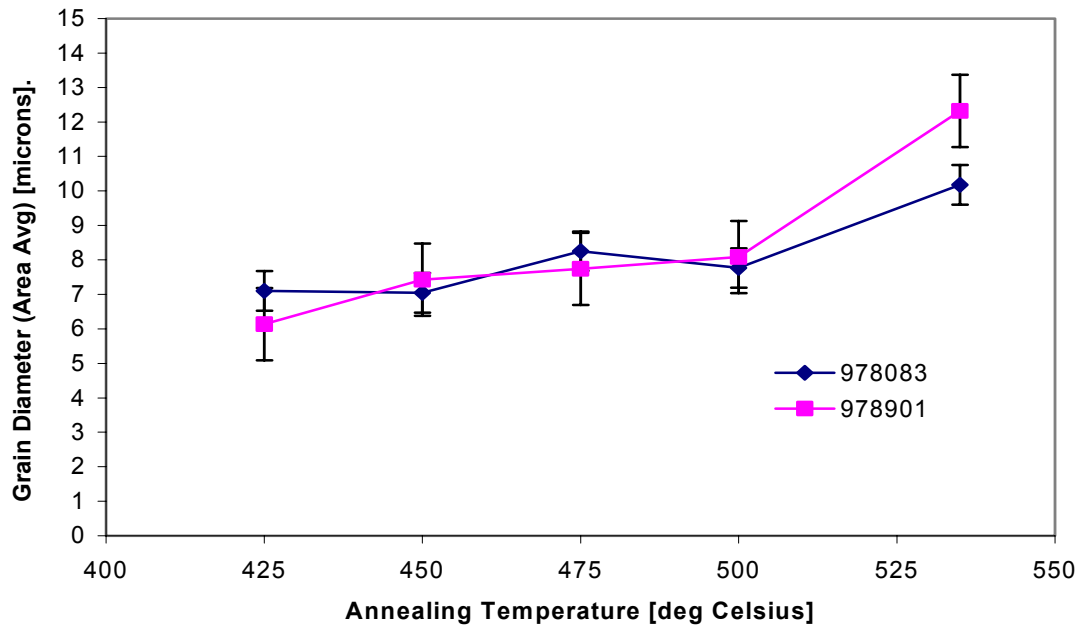


Figure 4.10. Area weighted grain diameter as a function of annealing temperature. Each data point is an average of four 100×100 micron scans with a step size of 1 micron. Standard error bars have been superimposed at each point. Variation in annealing temperature from 425 °C to 500 °C has only a minimal coarsening effect on grain size. Coarsening increases at 535 °C, suggesting that the best range of temperatures for superplastic forming lies between 425 °C and 500°C.

	425°C	450°C	475°C	500°C	535°C
978901	6.1	7.4	7.7	8.1	12.3
978083	7.1	7.0	8.3	7.8	10.02

Table 4.1 Average area weighted grain diameter in microns for 978901 and 978083 materials.

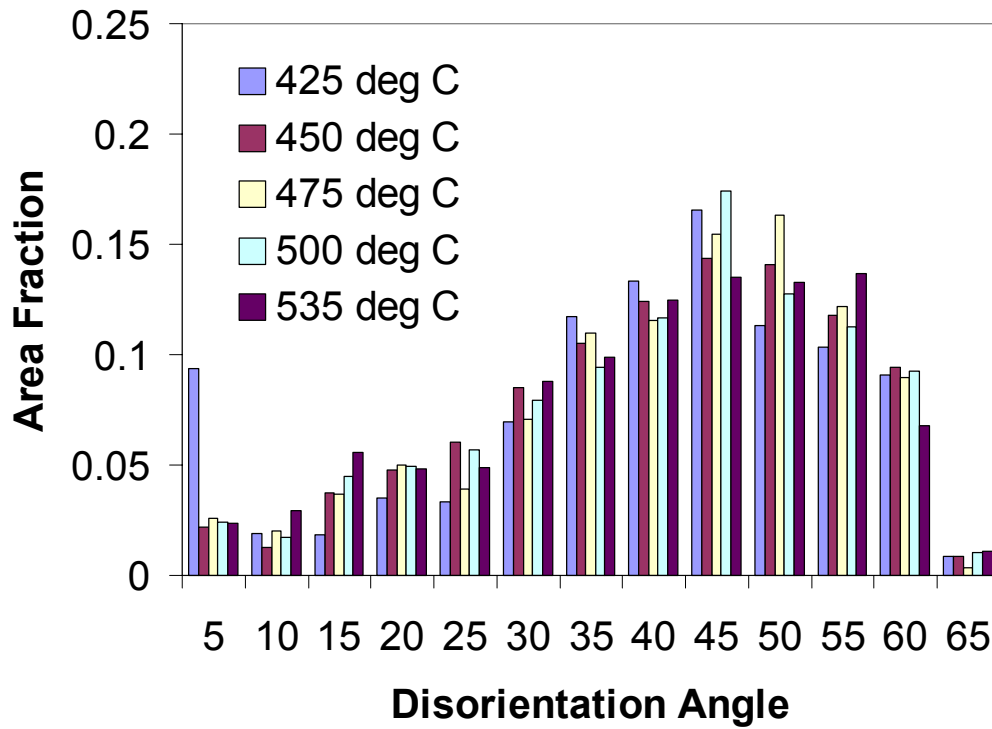


Figure 4.11. Disorientation histogram for 978901 material at various annealing temperatures. The histogram follows a Mackenzie distribution [Ref. 22] for randomly oriented grains and is rich in high angle boundaries at all temperatures. At 425 °C this material is not fully recrystallized (Figure 4.7).

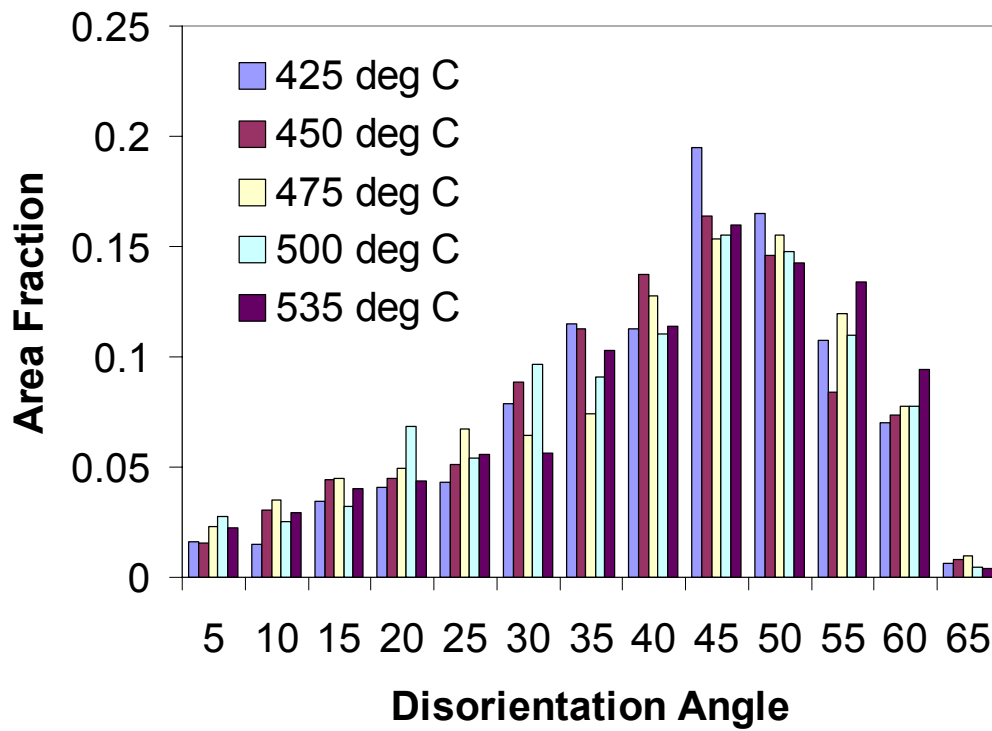
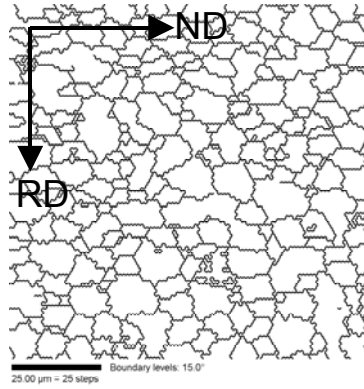
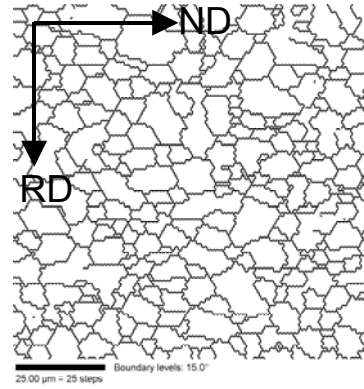


Figure 4.12. Disorientation histogram for 978083 material at various annealing temperatures. This material also follows a Mackenzie distribution [Ref. 22] for randomly oriented grains and is rich in high angle boundaries at all temperatures.



(a)



(b)

Figure 4.13. Grain boundaries with disorientations $\geq 15^\circ$ for (a) 978901 and (b) 978083 materials annealed at 500°C . A fine, equiaxed distribution of high angle boundaries is required for superplasticity. The microstructure in this representation is essentially the same as that shown in Figures 4.7(d) and 4.8(d), revealing that nearly all grain boundaries in the Figures 4.7(d) and 4.8(d) are capable of GBS.

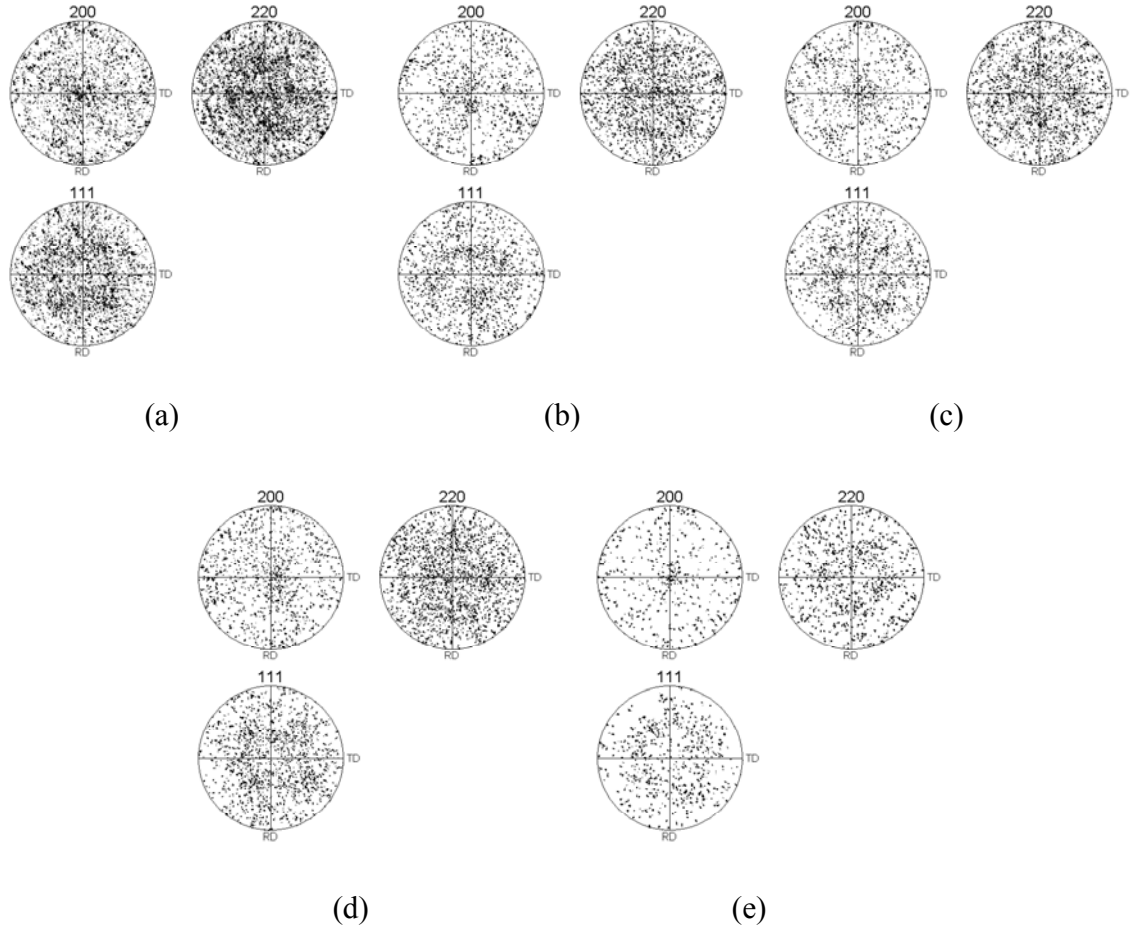


Figure 4.14. Discrete pole figures for the 978901 material annealed at the following temperatures: (a) 425°C, (b) 450°C, (c) 475°C, (d) 500°C, (e) 535°C. The pole figures for each annealing temperature comprise a random and cube-type texture component. The random component is due to particle-stimulated nucleation and is favorable for grain boundary sliding and superplastic behavior. The cube-type component may be due to high angle boundaries in the cold worked condition.

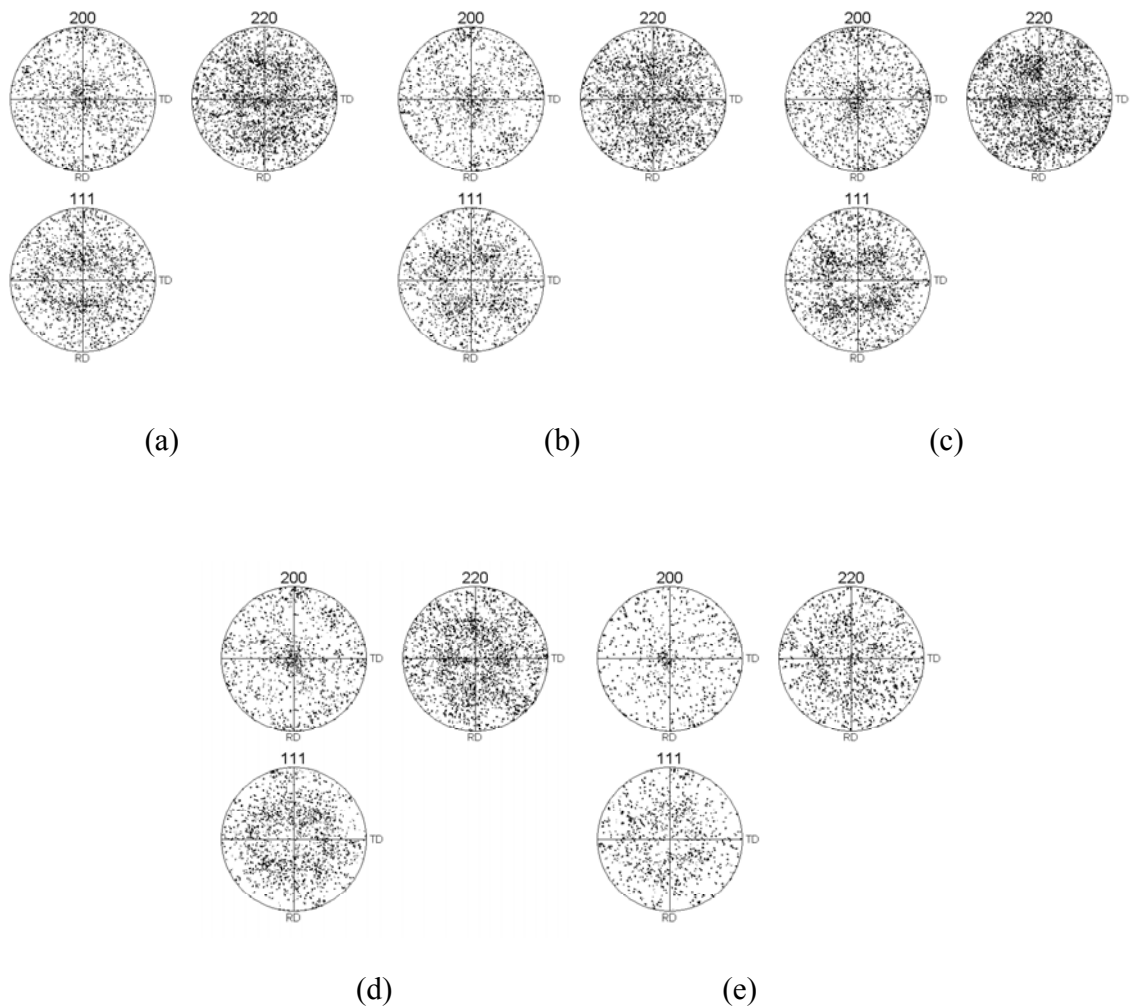


Figure 4.15. Pole figures for 978083 material annealed at the following temperatures: (a) 425 degrees C, (b) 450°C, (c) 475°C, (d) 500°C, (e) 535°C. The 978083 material behaves essentially the same as 978901 material (Figure 4.9), at all annealing temperatures.

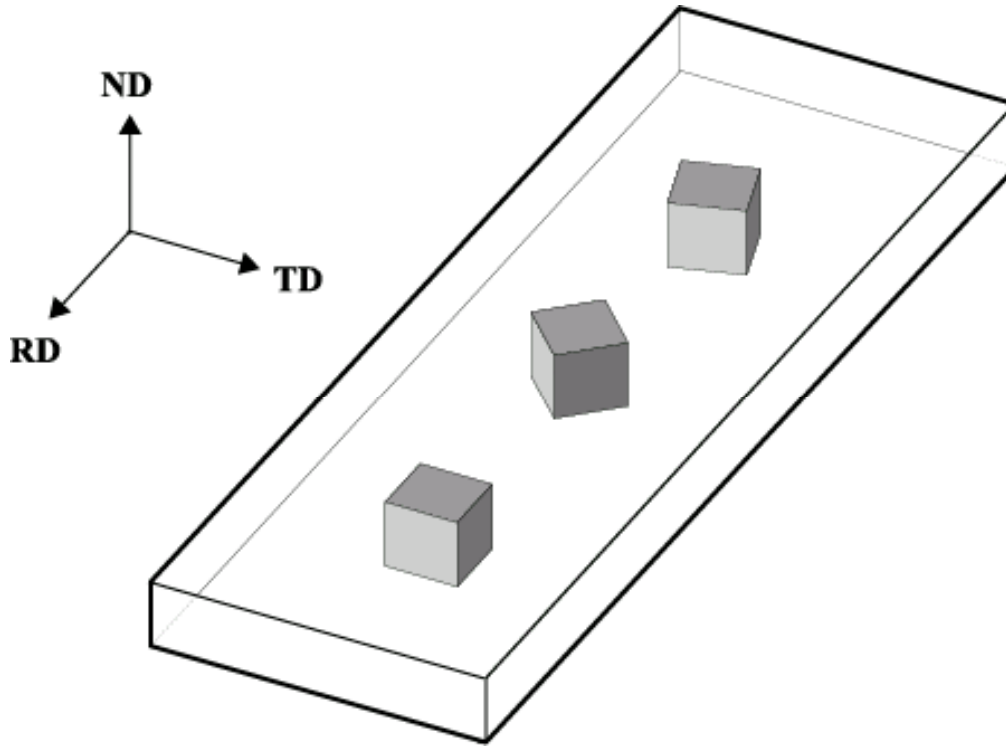


Figure 4.16 Schematic of cubic lattice orientations in 978901 or 978083 materials in annealed condition resulting from the weak cube-type component. This schematic reflects the tendency of the $\{100\}$ to align with the rolling plane although no low-index direction, such as $\langle 100 \rangle$, appears to align with the rolling direction

C. MECHANICAL TESTING OF 5083 ALUMINUM ALLOYS 978901 AND 978083

Taleff and Kulas [Ref. 21] conducted mechanical testing of the 978901 and 978083 AA5083 materials at the University of Texas at Austin. Test coupons were machined so that the tensile axis was parallel to the rolling direction of the as-received sheet. The results are summarized in Figure 4.17 in the form of plots of strain rate as a function of stress for various testing temperatures ranging from 425°C to 500°C. As discussed in Section II-B, two mechanisms may contribute independently (and therefore additively) to the elevated temperature deformation of a fine-grained material. A transition from GBS to dislocation creep, which is dominated by slip processes, may be observed on these graphs as a change in slope from a lower value, corresponding to $m \approx 0.5$, to a larger value, corresponding to $m \approx 0.2$. The region wherein the slope of these plots changes, near a strain rate of $\sim 1 \times 10^{-3} \text{ s}^{-1}$, is a transition region in which both mechanisms contribute to the deformation rate. This transition region extends over less than one order of magnitude in strain rate. According to the data in Figure 4.17, the maximum strain rate at which superplastic ductility is expected is approximately independent of temperature and is about $1 \times 10^{-3} \text{ s}^{-1}$. Maximum observed ductilities for each material are listed in Table 4.2.

From the current understanding of superplasticity, deformation at strain rates below this transition value will be dominated by GBS, while at higher strain rates deformation will occur by dislocation slip. These mechanisms are expected to result in different effects on the microstructure and texture of the initial, annealed condition of the material. Thus, for each material, OIM and microtexture analysis was performed on samples deformed at 500 °C and either at $3 \times 10^{-4} \text{ s}^{-1}$ (in the GBS regime) or $3 \times 10^{-2} \text{ s}^{-1}$ (in the dislocation creep regime). The data points corresponding to these deformation conditions have been highlighted on Figure 4.17.

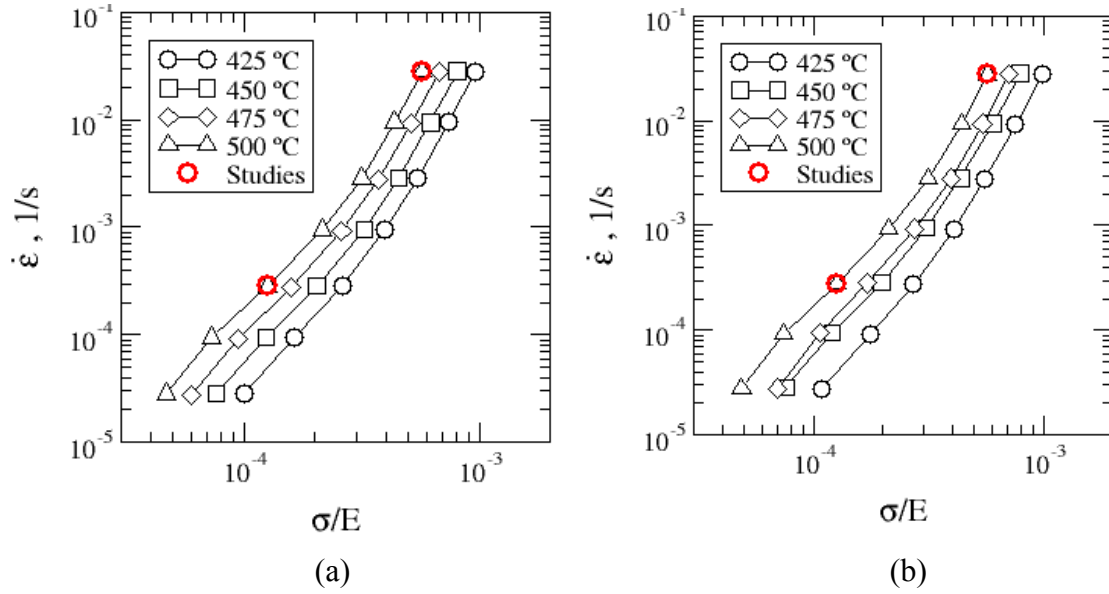


Figure 4.17 Strain rate as a function of stress for (a) 978901 and (b) 978083 materials. Mechanical testing performed at the University of Texas-Austin [Ref. 21]. A change in slope at about 10^{-3} s^{-1} reflects a transition from GBS to dislocation creep. Samples were selected from the GBS and dislocation creep regimes for further analysis. The red circles highlight these data points.

Material	S.P.F. % Elongation
978083	471
978901	237

Table 4.2. Maximum observed ductilities of 978901 and 978083 materials deformed at a strain rate of $3 \times 10^{-4} \text{ s}^{-1}$.

D. OIM AND MICROTEXTURE ANALYSIS OF 5083 ALUMINUM ALLOYS 978901 AND 978083 AFTER TENSILE DEFORMATION

Microtexture and OIM analysis were conducted on the 978901 and 978083 materials following deformation at a strain rate of $3 \times 10^{-4} \text{ s}^{-1}$. Samples were examined after various nominal strain values (50%, 100%, 150%, and 200%) in order to assess the evolution of the both microtexture and the microstructure as a function of strain. Unique grain color maps for 978901 material are shown in Figure 4.18. After 50% strain, the microstructure comprises a mixture of equiaxed grains and grains that are slightly elongated in the tensile (RD) direction. As strain increases, larger grains grow slightly and remain elongated in the tensile direction while the finer grains remain equiaxed and constant in size. At 200% tensile elongation, cavitation has become apparent; the dark regions of very low image quality are the cavities. Results for the 978083 material are presented in Figure 4.19; the evolution of microstructure during tensile extension to a strain of 200% for this material is essentially the same as in the 978901 material.

The strain rate for these samples is just below the rate for the apparent transition from GBS to dislocation creep and so these observations may be attributed to the combined effects of these two mechanisms. GBS would be expected to be the dominant mechanism, especially in regions of fine grain size wherein grains remain equiaxed in shape. Grain elongation in coarser grains would then be due to a contribution of dislocation creep to the local strain in the sample.

Dynamic grain growth during superplastic deformation by GBS is summarized in Figure 4.20 and Table 4.3 for the data of Figures 4.18 and 4.19. Again, the grain size value is the area weighted average grain diameter determined from the OIM data. From the mechanical testing procedures [Ref. 21] the heating time at 500°C prior to initiation of a test is about 1 hour. At a strain rate of 3×10^{-4} an additional elapsed time of about 30 min is required to attain a strain of 50% while nearly two hours additional elapsed time is required to attain a strain of 200%. At 50% elongation, the average grain diameter of the 978901 material is 11.5 μm and the average grain diameter of the 978083 material is 11.0 μm . These values are essentially the same and both are greater than the grain size following an equivalent annealing time of one hour, which was approximately 8.0 μm for

these two materials (Table 4.1). Thus, concurrent straining enhances grain growth, and grain size increases further with respect to strain at a rate of about 1 μm for every 50% strain up to 150% elongation. From 150% strain to 200% strain, grain growth continues in the 978901 material while it apparently stops in the 978083 material.

Further assessment of dynamic grain growth was conducted by examining the microstructure in the un-deformed grip section of the test sample of the 978083 material that had been deformed to 200% strain. This sample had experienced a total elapsed time at 500°C of nearly three hours and the resulting average grain size value was 8.6 μm . This material exhibited an average grain size of 7.8 μm (Table 4.1) after an annealing time of one hour at this temperature. Thus grain growth during straining occurs more rapidly than during comparable intervals of static annealing.

Microtexture data in the form of discrete pole figures for the samples of the 978901 and 978083 materials deformed 500°C and $3 \times 10^{-4} \text{ s}^{-1}$ are provided in Figure 4.21 for the 978901 material and 4.22 for the 978083 material. These data correspond to the images of Figures 4.18 and 4.19, respectively. Again, both materials exhibit essentially the same microstructural response for deformation up to approximately 200%. In both cases, the cube-type texture component observed in the annealed material has diminished during the initial stages of deformation and is not apparent at $\geq 50\%$ strain. No other texture components have appeared and the texture appears random. Randomization of texture is consistent with GBS dominated deformation as grains slide and rotate in order to accommodate elongation.

A similar OIM study of the 978901 and 978083 AA5083 materials during deformation at a higher strain rate of $3 \times 10^{-2} \text{ s}^{-1}$ was also conducted. These materials also exhibited different ductilities at this higher rate: the 978901 material failed at an elongation of 118% while 978083 material again accommodated nearly twice as much strain before failing at 220% elongation. Unique grain color maps for 97801 and 978083 materials deformed at $3 \times 10^{-2} \text{ s}^{-1}$ are provided in Figures 4.23 and 4.24. Deformation is now likely to be dominated by dislocation creep, with grains elongating in response to long-range motion of dislocations by glide and climb. However, Figure 4.23(a) shows a fine but equiaxed grain structure, which would be expected of a material deforming by

GBS. In this grain map, the grain tolerance angle had been set to a disorientation sensitivity of 2° . Figure 4.23(b) shows the same orientation data but with a grain tolerance angle that has been increased to 15° . Furthermore, boundaries of disorientation $\geq 30^\circ$ have been highlighted in the image of Figure 4.23(b). In this representation the microstructure now shows definite grain elongation in the tensile (RD) direction. This observation is consistent with dislocation creep. The glide motion of dislocations accounts for the strain while diffusion-controlled climb results in the formation of a subgrain structure within elongated grains that are surrounded by the high-angle boundaries.

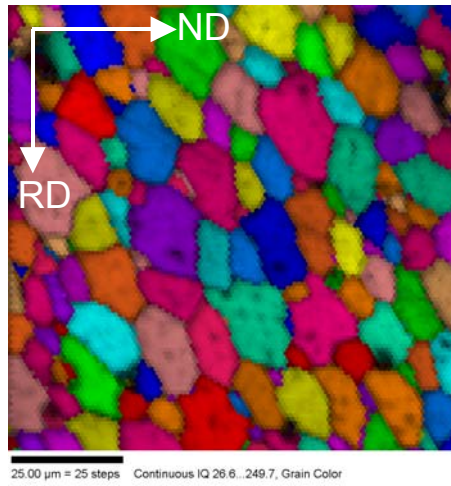
Further evidence for dislocation creep may be seen in the microtexture data shown in Figure 4.25 for the 978901 and 978083 materials following deformation at $3 \times 10^{-2} \text{ s}^{-1}$, i.e., in the dislocation creep regime. The data for the 978901 material (Figure 4.25(a)) were obtained after deformation to failure at 118% strain while the data for the 978083 material are for a sample deformed to approximately 200% elongation. Both materials exhibit a distinct deformation texture that is consistent with dislocation creep during tensile extension. There are two components in the deformation texture. A $\{001\}\langle 100 \rangle$ cube texture component is readily apparent in the concentration of orientations at the center and along both the RD and TD in the $\{200\}$ pole figures, while a $\langle 111 \rangle$ fiber orientation is apparent in the concentration of orientations along the RD in the $\{111\}$ pole figures and as bands approximately 35° and 90° from the RD in the $\{220\}$ pole figures. The strength of the $\langle 111 \rangle$ fiber appears stronger in the 978083 material; this may reflect the larger strain before failure of this material.

The formation of these two texture components during elevated temperature deformation of SKY5083 material has been examined by electron backscatter diffraction methods. In this work, it was shown that the $\langle 111 \rangle$ fiber texture component can form by slip-induced lattice rotation within grains in the random population in the texture. The $\{001\}\langle 100 \rangle$ cube component then reflects slip-induced lattice rotation in grains belonging to the $\{001\}\langle uv0 \rangle$ population. Furthermore, the grains having the $\langle 111 \rangle$ fiber orientation have six slip systems in three sets of conjugates with equal resolved shear stress while grains with the $\{001\}\langle 100 \rangle$ cube orientation have eight slip systems in four

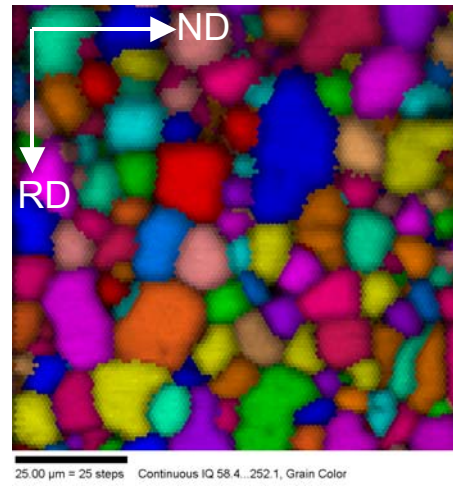
conjugate sets. Thus both of these components meet the Taylor requirement for a minimum of five independent slip systems, and, furthermore, grains with either of these orientations can deform in a mutually compatible manner during tensile elongation [Ref. 5].

Figures 4.26 and 4.27 provide histograms of the grain-to-grain disorientation angles for the 978901 and the 978083 materials, respectively. These histograms enable comparison of data for materials deformed to similar strains in either the dislocation creep regime (at $3 \times 10^{-4} \text{ s}^{-1}$) or the GBS regime (at $3 \times 10^{-2} \text{ s}^{-1}$). In both materials, the samples deformed in the GBS regime exhibit a Mackenzie-like random distribution dominated by high angle boundaries [Ref. 22]. The samples deformed in the dislocation creep regime (both samples were deformed to failure) exhibit populations of low-angle boundaries ($2^\circ - 15^\circ$) that reflect the formation of substructure in association with dislocation creep processes.

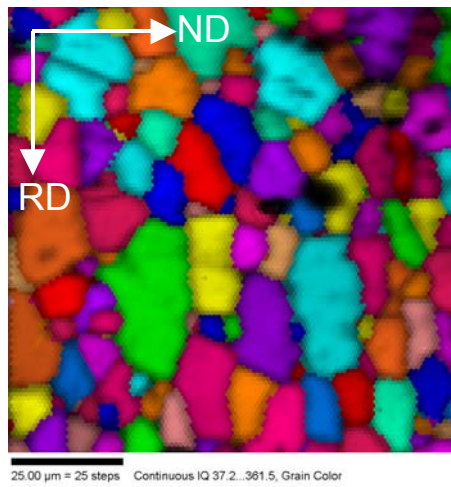
Altogether, these data demonstrate that OIM analysis is capable of determination of the local deformation modes in a material. Deformation behavior in regions as small as $25 \text{ }\mu\text{m}$ in extent may be accurately assessed and so OIM may be capable of evaluating variations in deformation behavior throughout a large component that may experience non-uniform stresses and strain rates. Superplastic deformation by GBS is reflected in the randomizing of texture while slip processes result in the formation of distinct deformation texture components. The deformation texture that forms will certainly be expected to depend on the initial texture of the material.



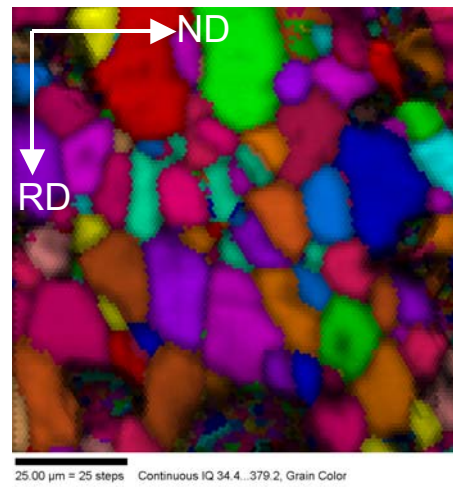
(a)



(b)

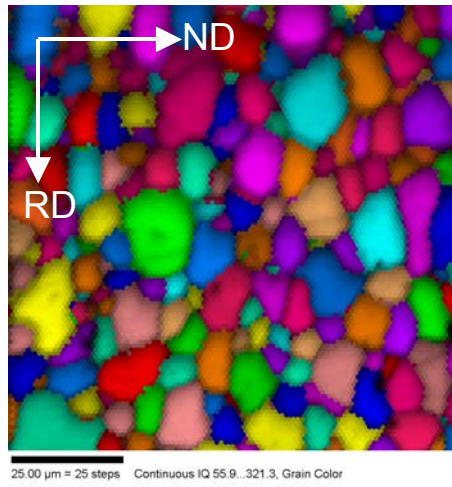


(c)

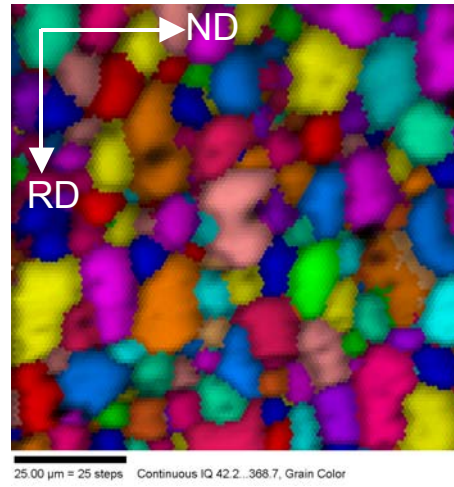


(d)

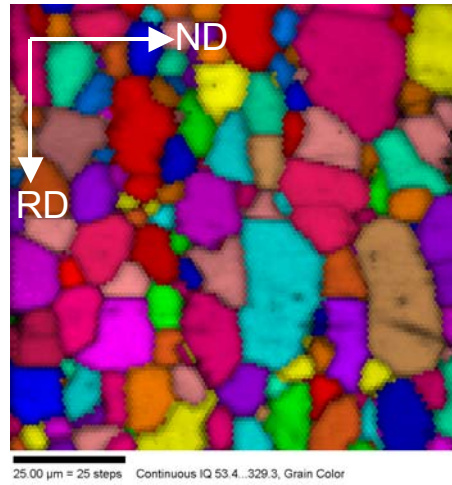
Figure 4.18. Unique grain color maps with image quality grayscale of 978901 material deformed at $3 \times 10^{-4} \text{ s}^{-1}$ and 500°C to nominal strains of (a) 50%, (b) 100%, (c), 150%, and (d) 200%. Grain structure remains essentially equiaxed, but some elongation in the RD direction is evident at all strain levels. The strain rate for these samples is just below the apparent transition point for GBS. Slight elongation may be attributed to contribution of dislocation creep. Some cavitation is evident in (d) indicated by dark regions of very low IQ.



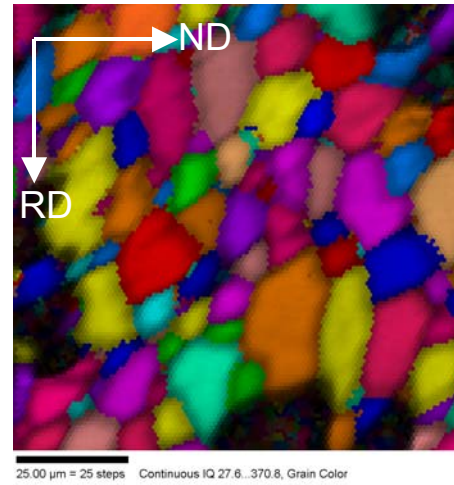
(a)



(b)



(c)



(d)

Figure 4.19. Unique grain color maps with image quality grayscale of 978083 material deformed at $3 \times 10^{-4} \text{ s}^{-1}$ and 500°C to nominal strains of (a) 50%, (b) 100%, (c), 150%, and (d) 200%. Microstructure is essentially identical to 978901 material (Figure 4.17).

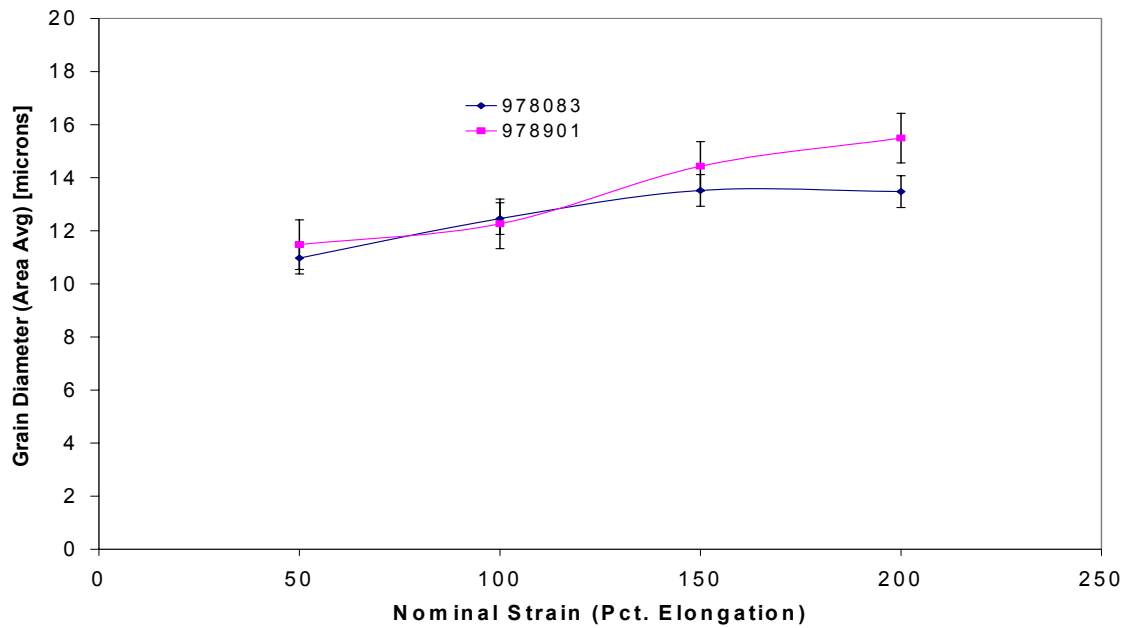
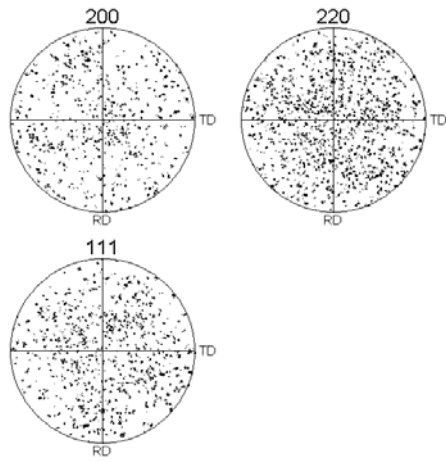


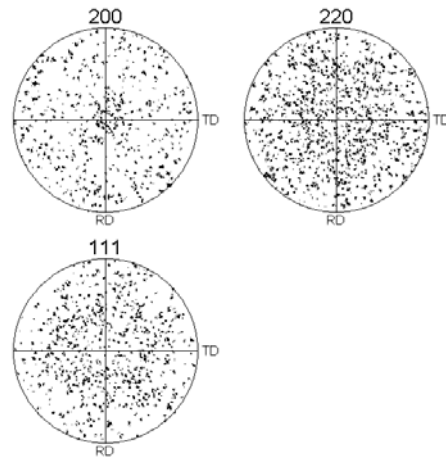
Figure 4.20. Area weighted grain diameter as a function of stain in 978901 and 978083 materials deformed at a strain rate of 3×10^{-4} , 500°C. Each data point is an average of at least two 100 μm x 100 μm scans with a 1 μm step size. Standard error bars have been superimposed at each point. Gradual coarsening occurs as strain increases, a result of the contributions of dislocation slip deformation. The 978901 material, closer to its failure ductility, coarsens slightly more than the 978083 material.

	50%	100%	150%	200%
978901	11.5	12.3	14.4	15.5
978083	11	12.5	13.5	13.5

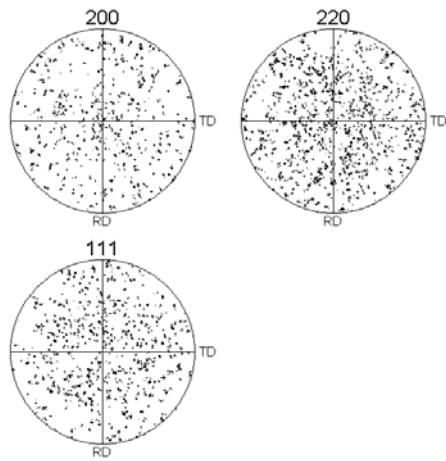
Table 4.3. Average area weighted grain diameter in microns for 978901 and 978083 materials.



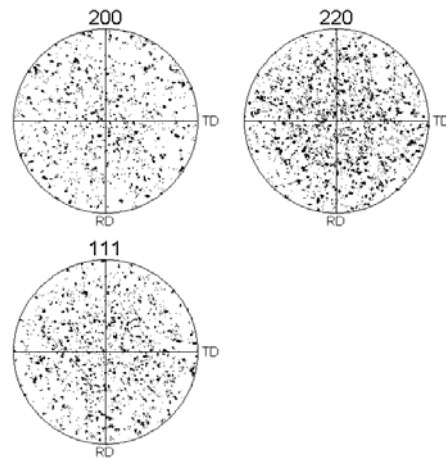
(a)



(b)

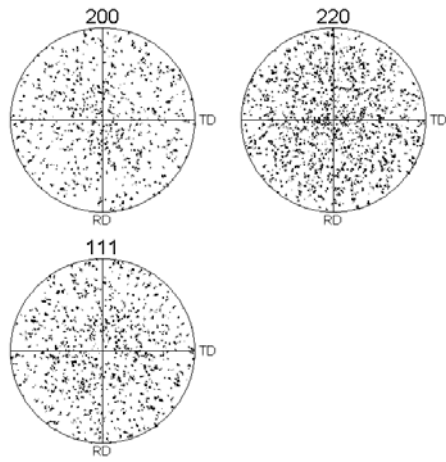


(c)

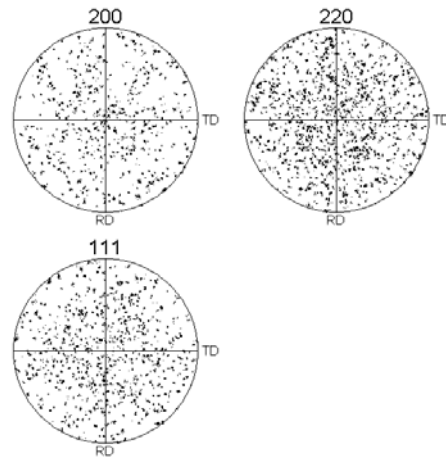


(d)

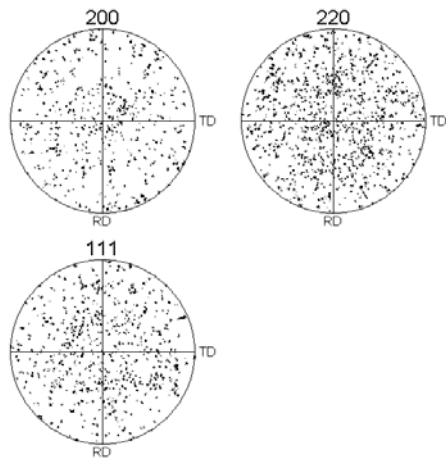
Figure 4.21. Discrete pole figures for 978901 material deformed at 3×10^{-4} to (a) 50%, (b) 100%, (c) 150%, (d) 200% elongations. In all cases the texture has been randomized. This randomization indicates that the dominant deformation mechanism is GBS [Ref. 5].



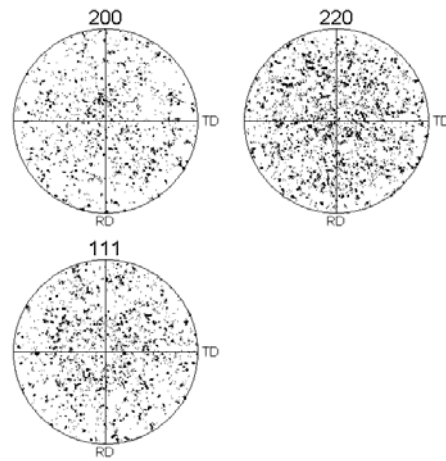
(a)



(b)



(c)



(d)

Figure 4.22. Discrete pole figures for 978083 material deformed at 3×10^{-4} to (a) 50%, (b) 100%, (c) 150%, (d) 200% elongations. As in the 978901 material (Figure 4.21), the texture has been randomized at all strains.

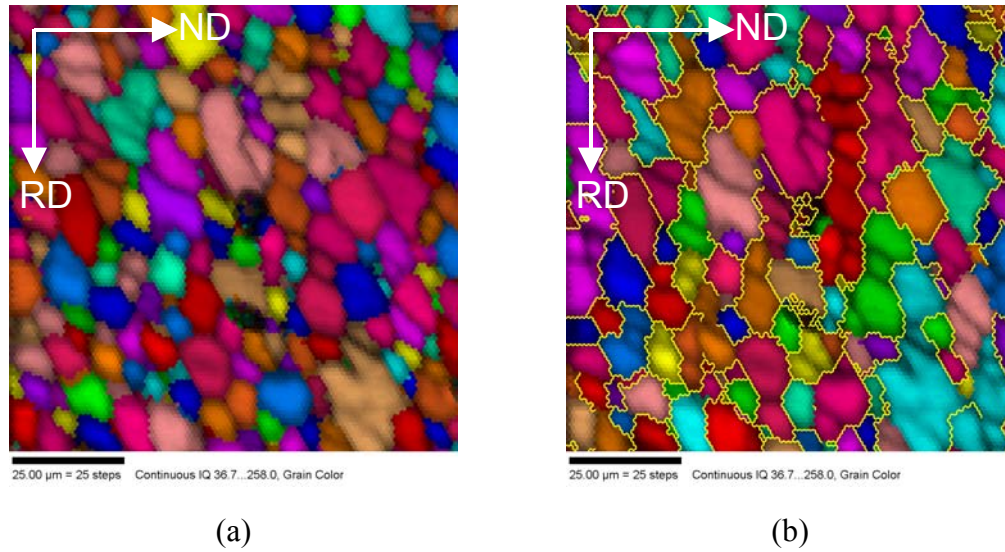


Figure 4.23. Unique grain color maps for 978901 material deformed at $3 \times 10^{-2} \text{ s}^{-1}$ and 500°C to 118% strain with superimposed image quality grayscale. Grain tolerance angle in (a) is 2° . The microstructure in (a) is not elongated, as suggested by dislocation creep theory [Ref. 5]. However, when grain tolerance angle is increased to 15° (b), the structure now appears elongated in the rolling direction. High angle boundaries of disorientation greater than 30° have been highlighted yellow. Diffusion-controlled climb results in the formation of a subgrain structure within elongation grains that are surrounded by the high-angle boundaries

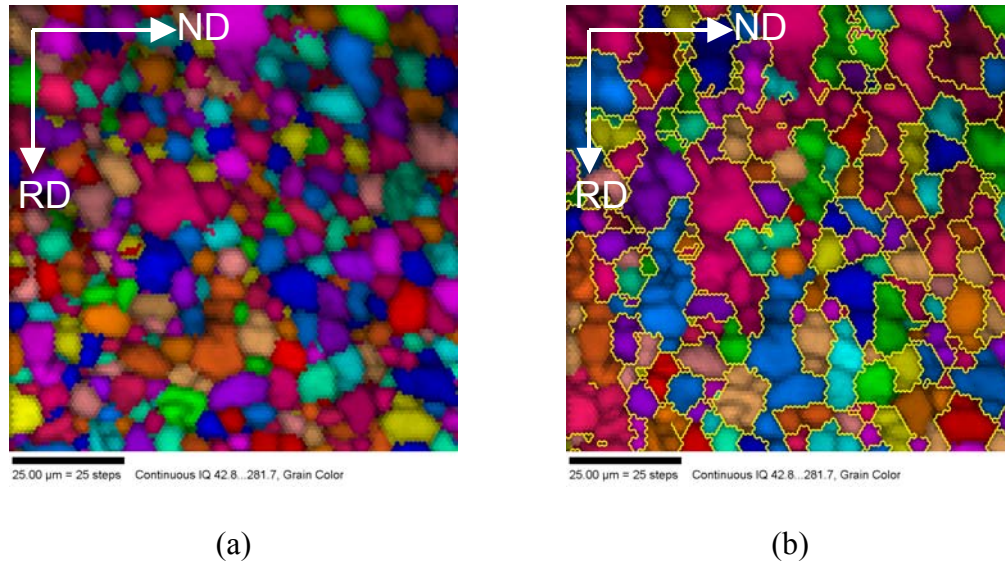


Figure 4.24. Unique grain color maps for 978083 material deformed at $3 \times 10^{-2} \text{ s}^{-1}$ strain rate and 500°C with superimposed image quality grayscale. Grain tolerance angle in (a) is 2° and in (b) is 15° to show elongation with respect to the higher angle boundaries. The results here are essentially the same as 978901 material in Figure 4.23.

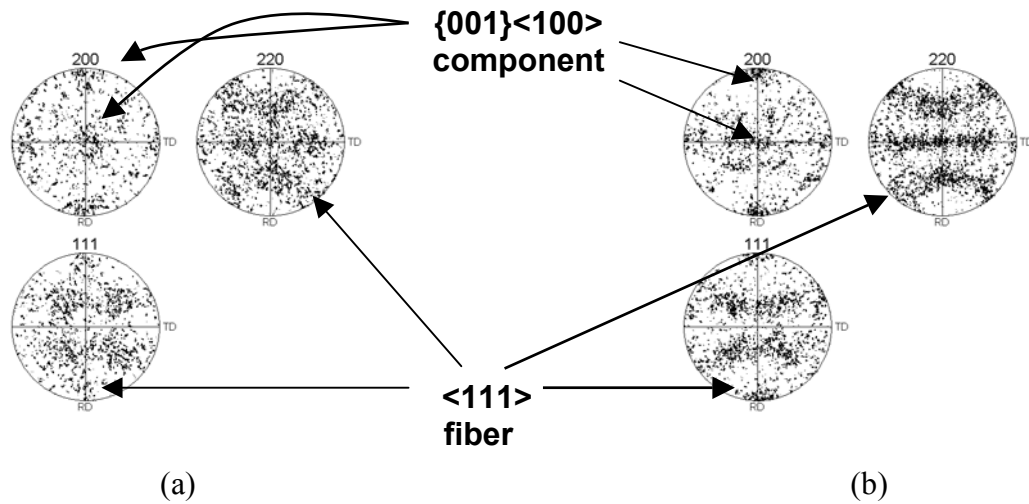


Figure 4.25. Discrete pole figures for (a) 978901 and (b) 978083 materials deformed at $3 \times 10^{-2} \text{ s}^{-1}$. Both material's now exhibit preferred orientation including a $\{001\} \langle 100 \rangle$ component and a $\langle 111 \rangle$ fiber. The 978083 material has a stronger $\langle 111 \rangle$ fiber texture than the 978901 material. The formation of these textures confirms that dislocation creep is the dominant deformation mechanism at this strain rate and temperature [Ref. 5].

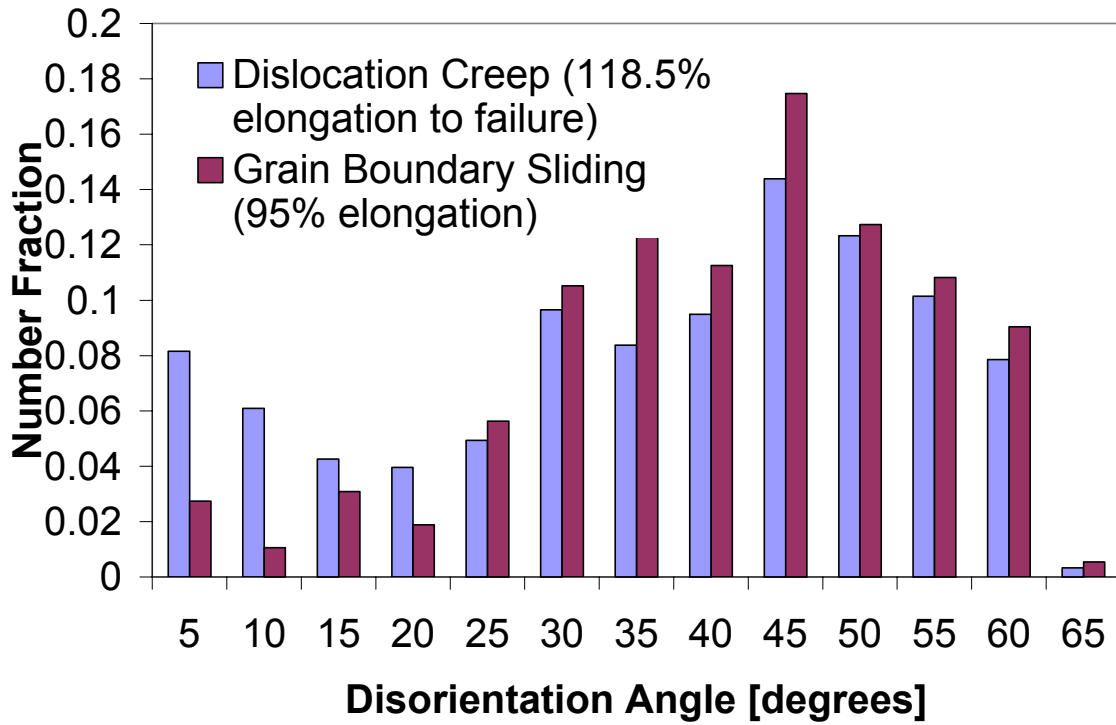


Figure 4.26. Disorientation distribution histogram for 978901 material deformed at $3 \times 10^{-4} \text{ s}^{-1}$ (GBS) and $3 \times 10^{-2} \text{ s}^{-1}$ (dislocation creep) strain rates. The sample deformed in the GBS regime exhibits a Mackenzie-like random distribution dominated by high angle boundaries [Ref. 22]. The sample deformed in the dislocation creep regime (to failure) exhibits populations of low-angle boundaries (2° - 15°) that reflect the formation of substructure in association with dislocation creep processes.

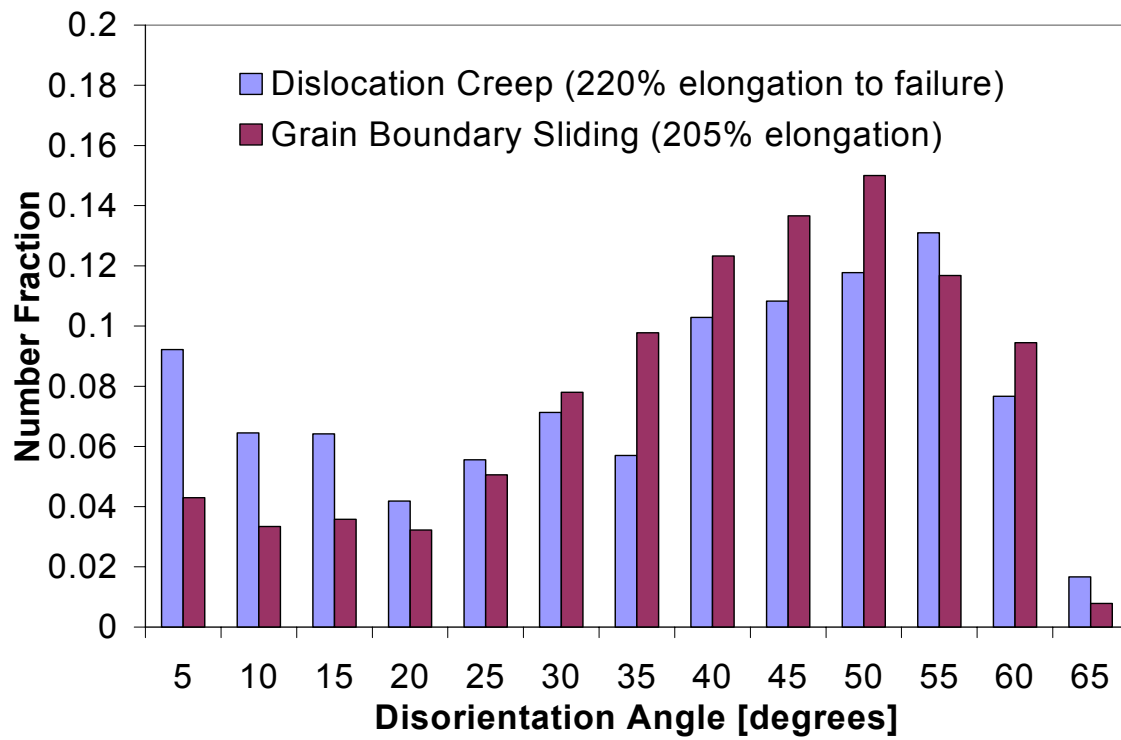


Figure 4.27. Disorientation distribution histogram for 978083 material deformed at $3 \times 10^{-4} \text{ s}^{-1}$ (GBS) and $3 \times 10^{-2} \text{ s}^{-1}$ (dislocation creep) strain rates. The data is essentially the same as demonstrated by the 978901 material (Figure 4.26)

E. OIM AND MICROTTEXTURE ANALYSIS OF SKY 5083 ALUMINUM ALLOYS AFTER TENSILE DEFORMATION

The available samples of SKY5083 material that had been deformed at 535°C and strain rates of either $1 \times 10^{-4} \text{ s}^{-1}$, $1 \times 10^{-3} \text{ s}^{-1}$, $1 \times 10^{-2} \text{ s}^{-1}$, or $1 \times 10^{-1} \text{ s}^{-1}$ permitted analysis of the microstructure and microtexture changes over this wider range of strain rates. Mechanical property data [Ref. 5] indicated that the lower two strain rates correspond to deformation in the GBS regime while deformation at the higher rates falls within the dislocation creep regime. Results of OIM analysis of the SKY material are summarized in Figures 4.28 and 4.29. This material exhibits essentially the same response as did the 978901 and 978083 materials and extends this observation over a wider range of strain rates. The unique grain color maps in Figure 4.28(a) and (b) illustrate that deformation at rates within the superplastic regime results in coarsening accompanied by slight elongation of the grains. The extent of coarsening is less at a higher strain rate, although the ductility is also less. A random texture, formed by random grain rotations during GBS deformation, is seen in the accompanying pole figures below the grain maps. The disorientation distributions shown in Figure 4.29 are similar to the Mackenzie random distribution [Ref. 22] but there are also populations of low-angle boundaries that exceed random. For deformation at the strain rates within the dislocation creep regime, Figure 4.28(c) and (d), the apparent grain size is finer but also remains equiaxed in appearance. This was also the case for OIM analysis of the 978901 and 978083 materials, as shown in Figures 4.23(a) and 4.24(a). The corresponding pole figures in Figure 4.28(c) and (d) also reveal both a $\{100\}\langle 001 \rangle$ cube component and a $\langle 111 \rangle$ fiber component in the texture associated with deformation in the dislocation creep regime. In Figure 4.29, the disorientation distribution histograms also indicate a distinct increase in population of low-angle ($2^\circ - 15^\circ$) boundaries that may be associated with subgrain formation. If the grain tolerance angle is increase from 2° to 15° the unique grain color maps reveal grain elongation, as shown in Figure 2.28 for the SKY5083 deformed at the higher two strain rates of $1 \times 10^{-2} \text{ s}^{-1}$ and $1 \times 10^{-1} \text{ s}^{-1}$. Deformation at these faster strain rates results in the development of larger populations of low-angle boundaries, suggesting that they are a product of dislocation glide followed by diffusion controlled climb.

It is evident from Figures 4.28 and 4.29 that for each representation (grain maps, pole figures, and disorientation histograms), the observed characteristics of deformation vary in a predictable manner with strain rate. Deformation textures that are related to slip processes develop gradually with strain for strain rates above that for transition from GBS to dislocation creep. Grain elongation under dislocation creep conditions may be documented if the formation of substructure is taken into account. Conversely, grain coarsening occurs gradually with strain for strain rates below the transition. This is accompanied by randomizing of the texture. Altogether, the results of this investigation suggest that quantitative assessments of the deformation mechanisms could be developed and used to generate a scaling system wherein the relative contributions of dislocation creep and GBS may be evaluated in a superplastically formed component. This, in turn, may contribute to the validation of models for the forming of such components.

At the highest strain rate in this SKY study ($1 \times 10^{-1} \text{ s}^{-1}$) the sample exhibited an extended neck that involved essentially all of the gage length of the sample. Thus, the local strain determined from the reduction in cross-sectional area along the gage length of such a sample will vary continuously and differ from the nominal strain. This would allow determination of the dependence of texture strength on local strain during deformation under dislocation creep conditions. Results of this analysis are shown in Figure 4.30. The dimensions of the gauge section were approximated by assuming that the sample width varied linearly along the length in the region where material had already been sectioned away. OIM scans were completed at the indicated points along the gage length and showed that both of $\{100\}\langle 111 \rangle$ cube component and $\langle 111 \rangle$ fiber texture components developed everywhere but that their intensity varied with local strain. Again, quantitative measurement of texture strength may serve as an indicator of local strain as well as the deformation conditions in superplastic material undergoing deformation dominated by dislocation creep.

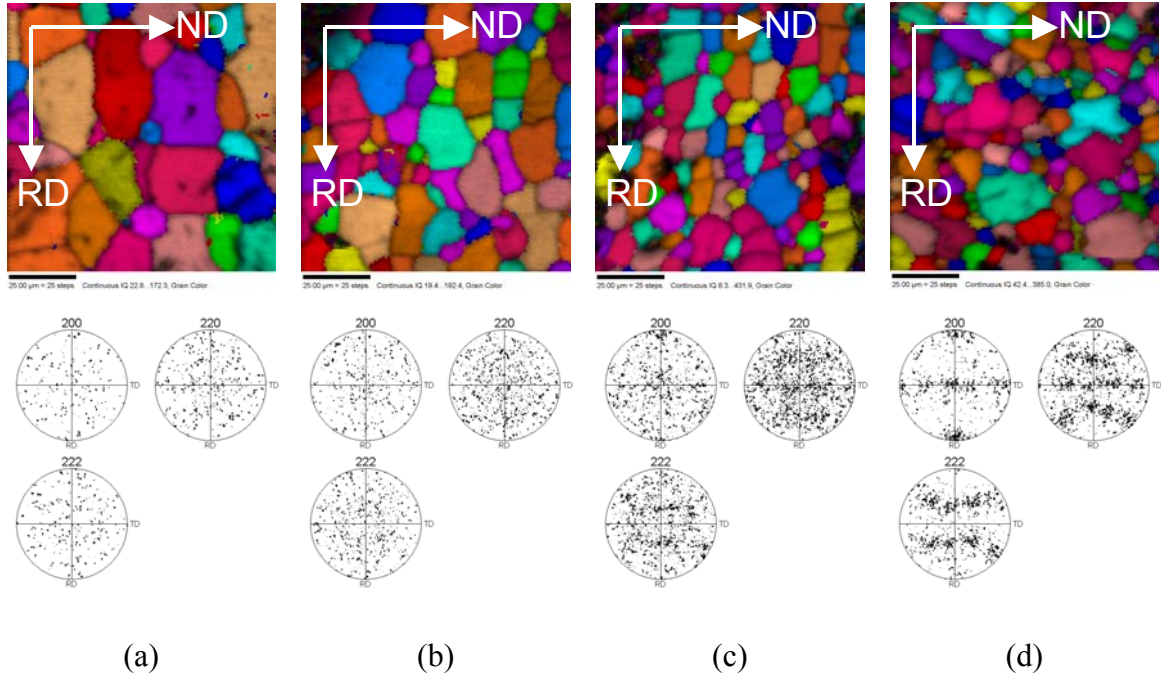


Figure 4.28. Unique grain color maps with image quality grayscale and pole figures of SKY material deformed at (a) $1 \times 10^{-4} \text{ s}^{-1}$, (b) $1 \times 10^{-3} \text{ s}^{-1}$, $1 \times 10^{-2} \text{ s}^{-1}$, and $1 \times 10^{-1} \text{ s}^{-1}$ strain rates at 535°C . All scans are $100 \mu\text{m} \times 100 \mu\text{m}$ with a $1 \mu\text{m}$ step size. This material exhibits essentially the same response as did the 978901 and 978083 materials but over a wider range of strain rates. In the dislocation creep regime, (c) and (d), the cube $\{001\}\langle 100 \rangle$ component and the $\langle 111 \rangle$ fiber component in the texture sharpen as strain rate is increased.

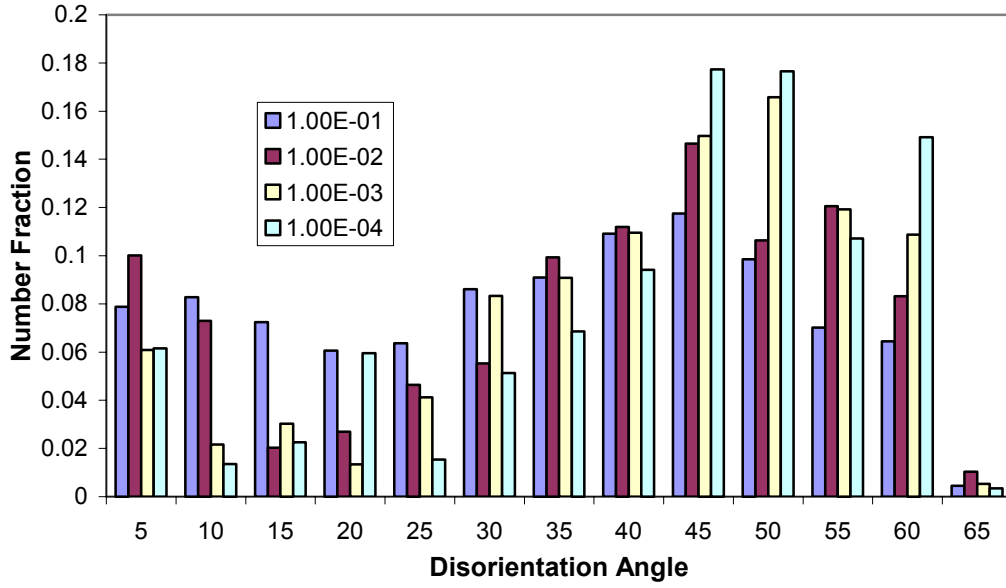


Figure 4.29. Disorientation distribution histogram for SKY material deformed at (a) $1 \times 10^{-4} \text{ s}^{-1}$, (b) $1 \times 10^{-3} \text{ s}^{-1}$, $1 \times 10^{-2} \text{ s}^{-1}$, and $1 \times 10^{-1} \text{ s}^{-1}$ strain rates at 535°C . This behavior is similar to 978901 and 978083 material (Figures 4.26 and 4.27). Material deformed under GBS dominated conditions results in a Mackenzie-like distribution [Ref. 22]. Materials deformed under dislocation creep dominated conditions have a higher percentage of low angle boundaries.

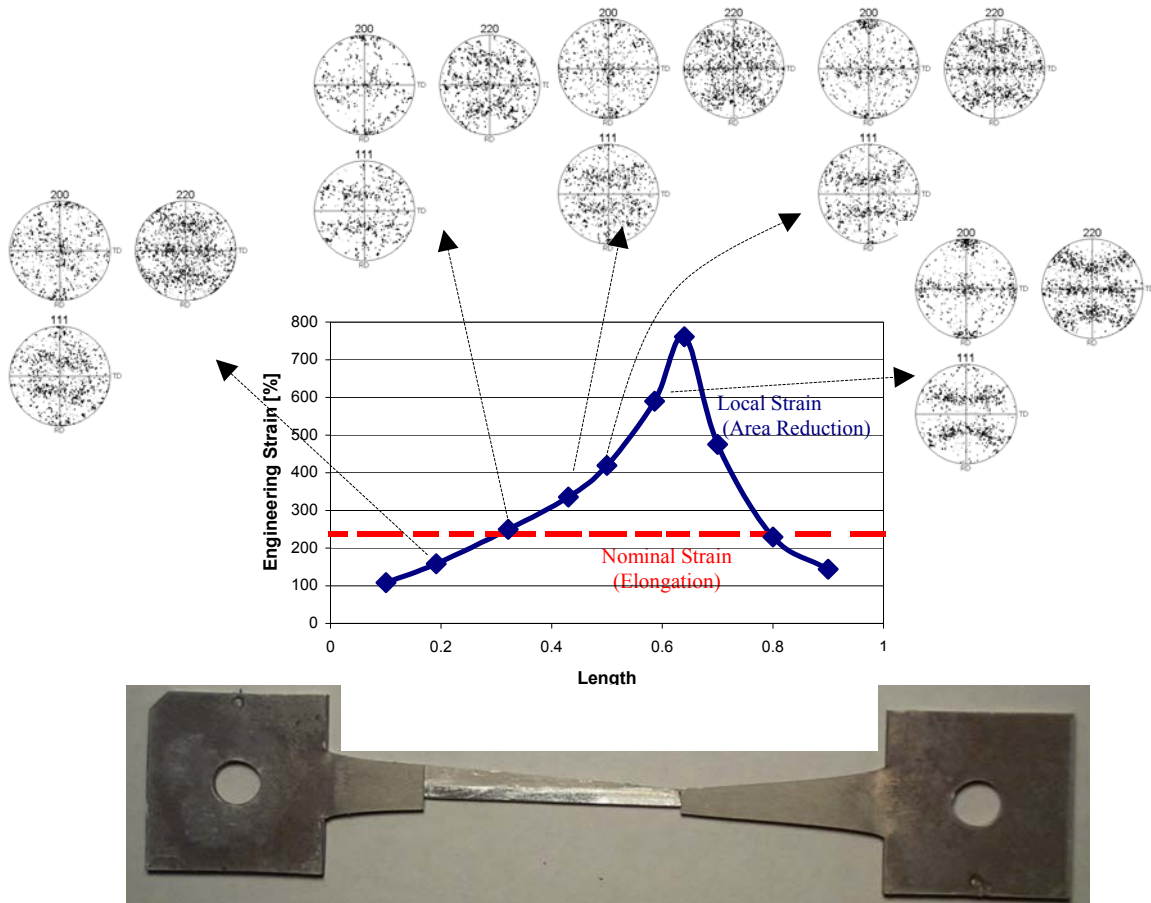


Figure 4.30. Discrete pole figures for SKY material deformed at 1×10^{-1} as a function of local strain. At this strain rate, the test sample undergoes some necking prior to failure. OIM scans were performed along the length of the sample to examine the effects of local strain. The intensity of the $\{100\}\langle 111 \rangle$ component and the $\langle 111 \rangle$ fiber increases with increasing local strain.

THIS PAGE INTENTIONALLY LEFT BLANK

V. CONCLUSIONS

A. CONCLUSIONS

1. The as-received 978901 and 978083 AA5083 materials were in a cold rolled condition. Both materials exhibited an elongated and banded structure and a B-type deformation texture.
2. Annealing of the 978901 and 978083 AA5083 materials at temperatures from 425°C to 500°C resulted in recrystallization and a fine-grained (6 μm – 8 μm) structure capable of supporting superplastic response. Recrystallized grain sizes, textures and the grain boundary disorientation distributions of these two materials were essentially identical. The textures were predominantly random and both had an abundance of high angle boundaries.
3. Transitions apparent in mechanical property data and OIM data reflect independent contributions of grain boundary sliding and dislocation creep mechanisms.
4. OIM and microtexture analysis are capable of detecting local deformation mechanisms in components undergoing superplastic forming. Strength of texture is an indicator of local deformation conditions.
 - a. Grain boundary sliding is indicated by texture randomization and moderate grain growth with slight elongation in the direction of applied stress.
 - b. Dislocation creep is indicated by fiber texture formation and a fine subgrain within elongated grains surrounded by high angle boundaries.
5. Texture intensity from OIM analysis can be employed as a measure of local strain under dislocation creep mechanisms.
6. The 978901 and 978083 materials exhibited essentially the same microstructure and microtexture in as-received, annealed, and deformation

conditions reviewed in this study. Therefore, the difference in observed ductility cannot be attributed to differences in microstructure or microtexture. The difference in ductility may be attributed to cavitation.

B. APPLICATION OF OIM TO MODELING OF SUPERPLASTIC RESPONSE

Determination of dominant deformation mechanisms in a deformed material may be accomplished by evaluation mechanical property data as suggested in Figure 2.1. However, this approach requires the execution of several tests to construct a plot to determine the transition point where the slope of the curve changes. An alternative approach, suggest in this work, is to assess the texture changes associated with the deformation of the material. As summarized in Figure 4.29, examination of texture will reveal the deformation regime. In this study, all samples were deformed at a uniform strain rate. A part that has been formed on a die will typically experience different strain rates at different points, resulting in varying mechanical response (and post-forming properties) in the same component. OIM analysis of a formed part would be useful in assessing the deformation mechanisms and the validity of models for the superplastic forming process.

C. RECOMMENDATIONS FOR FURTHER STUDY

1. Application of OIM and microtexture analysis to a wider range of superplastic materials, processing conditions and microstructures.
2. Quantitative measurement of texture intensity at varying strain rates and local strains.
3. Extension of OIM and microtexture to failure mechanisms to assess initiation of cavitation and at the point at which cavity linkage and failure occurs.
4. Application to a component undergoing superplastic forming to determine local deformation mechanisms.
5. Validation of models proposed to describe superplastic behavior.

THIS PAGE INTENTIONALLY LEFT BLANK

LIST OF REFERENCES

1. Ashby, M. F., *Acta Met.*, v. 37, pp.1273-1293, 1989.
2. Nieh, T.G., Wadsworth, J., and Sherby, O.D., *Superplasticity in Metals and Ceramics*. Cambridge University Press, New York, 1997.
3. McNelley, T.R, and McMahon, M.E., *Journal Of Metals*, v. 48, 2, 1996.
4. McNelley, T.R., McMahon, M.E., and Hales, S.J., *Scripta Materialia*, v .36, p.369, 1997.
5. Pérez-Prado, M.T., González-Doncel, G., Ruano, O.A., and McNelley, T.R., *Acta Materialia*, v. 49, p. 2259, 2001.
6. Poirier, J. P., *Creep of Crystals*. Cambridge University Press, p. 79, 1985.
7. Ruano, O. A., Miller, A. K., and Sherby, O.D., *Mater. Sci. Eng.*, v. 51, p.9, 1981.
8. Sherby, O.D. and Ruano, O.A., *Superplastic Forming of Structural Alloys*, ed. N.E. Patton and C. H. Hamilton, TMS-AIME, New York, 1982, p241.
9. Ruano, O.A. and Sherby , O.D., *Rev. Metal, Madrid*, v.19, p.261, 1983.
10. Gifkins, R.C., *Metall. Trans.*, v. 7a, p. 1225, 1976.
11. Ball, A. and Hutchison, M. M., *Met. Sci. J.*, v. 3, p. 1, 1969.
12. Sherby, O.D and Wadsworth, J., *Deformation Processing and Structure*, p.355, 1984.
13. Kokawa, H., Watanabe, T., and Karashima, S., *Phil. Mag. A*, v. 44, p. 1239, 1981
14. Doherty, R. D., Hughes, D. A., Humphreys, F.J., Jonas, J.J., Juul Jensen, D., Kassner, M. E., King, W. E., McNelly, T. R., McQueen, H. J. and Rollett, A. D., *Mater. Sci. Eng.*, v. A238, p. 219, 1997.
15. Waldman, J., Sulinski, H. and Markus, H., *Metall. Trans. A*, v. 5, p. 573, 1974.
16. Wert, J. A., Paton, N. E., Hamilton, C. H. and Mahoney, M. W., *Metall. Trans A*, v. 12A, p. 1267, 1981.
17. Humphreys, F. J., *Acta metal.*, v. 25, p.1323, 1977.

18. Chung, J.W. and Cahoon, J.R., "Superplasticity in Aluminum-Silicaon Eutectic," *Metal Sci.*, p. 13, 1979.
19. Randle, V., *Microtexture Determination and Its Applications*, The Institute of Materials, 1992.
20. Bunge, H.J., *Texture Analysis in Materials Science*, Butterworths, 1982.
21. Taleff, E.F. and Kulas, M. A., Private Communication, July, 2001.
22. Mackenzie, J.K., *Biometrika*, v.45, p.229, 1958.
23. Barrett, C.S., *Trans. Am. Inst. Min. Engrs.*, v. 135, p. 296, 1939.
24. Barrett, C.S. and Levenson, L.H., *Trans. Am. Inst. Min. Engrs.*, v. 137, p. 112-127, 1940.
25. Lee, C.S., Duggan, B.J., and Smallman, R.E., *Acta Metall. Mater.*, v. 41, p. 2265, 1993.
26. Lee, C.S. and Duggan, B.J., *Acta Metall. Mater.*, v. 41, p. 2691, 1993.
27. Lee, C.S., Duggan, B.J., and Smallman, R.E., *J. Phys. IV*, v. C7, p. 2027, 1993.
28. Lee, C.S., Smallman, R.E., and Duggan, B.J., *Scripta Metall. Mater.*, v. 33, p. 72, 1995.
29. Kulkarni, K., Starke, E.A. Jr., Kuhlmann-Wilsdorf, D., *Acta Mater.*, v. 46, p. 5283, 1998.
30. Swisher, D.L., *Production of Ultra-Fine Grains and Evoulution of Grain Boundaries During Sever Plastic Defomation of Aluminum and it Alloys*, Master's Thesis, Naval Postgraduate School, Monterey, CA, December 2000.
31. Juul Jensen, D., *Acta Metal.*, v. 43, p. 4117, 1995.

INITIAL DISTRIBUTION LIST

1. Defense Technical Information Center
Ft. Belvoir, VA
2. Dudley Knox Library
Naval Postgraduate School
Monterey, CA
3. Engineering and Technology Curricular Office, Code 34
Naval Postgraduate School
Monterey, CA
wtmccoy@nps.navy.mil
4. Department Chairman, Code ME/Mc
Naval Postgraduate School
Monterey, CA
tmcnelley@nps.navy.mil
5. Professor Terry R. McNelley, Code ME/Mc
Naval Postgraduate School
Monterey, CA
tmcnelley@nps.navy.mil
6. Professor Eric Taleff
The University of Texas at Austin
Austin, TX
taleff@mail.utexas.edu
7. Dr. Paul E. Krajewski
General Motors Corp.
Warren, MI
pkrajews@gmr.com
8. LT James W. Harrell
Naval Postgraduate School
Monterey, CA
harrellcb@cs.com